Ore Geology Reviews 136 (2021) 104260

Contents lists available at ScienceDirect

Ore Geology Reviews

journal homepage: www.elsevier.com/locate/oregeorev

# Texture, trace elements, sulfur and He-Ar isotopes in pyrite: Implication for ore-forming processes and fluid source of the Guoluolongwa gold deposit, East Kunlun metallogenic belt

Xing-Hui Li [a,b], Hong-Rui Fan [a,b,c,*], Gai-Zhong Liang [a,c], Ri-Xiang Zhu [b,c,d], Kui-Feng Yang [a,b,c], Matthew Steele-MacInnis [e], Huan-Long Hu [f]

[a] Key Laboratory of Mineral Resources, Institute of Geology and Geophysics, Chinese Academy of Sciences, Beijing 100029, China
[b] Innovation Academy for Earth Science, Chinese Academy of Sciences, Beijing 100029, China
[c] College of Earth and Planetary Science, University of Chinese Academy of Sciences, Beijing 100049, China
[d] State Key Laboratory of Lithospheric Evolution, Institute of Geology and Geophysics, Chinese Academy of Sciences, Beijing 100029, China
[e] Department of Earth and Atmospheric Sciences, University of Alberta, Edmonton, AB T6G 2E3, Canada
[f] State Key Laboratory of Ore Deposit Geochemistry, Institute of Geochemistry, Chinese Academy of Sciences, Guiyang 550081, China

ARTICLE INFO

*Keywords:*
Pyrite
Trace element
*In-situ* sulfur isotope
He-Ar isotopes
Magmatic-hydrothermal fluid

ABSTRACT

The Gouli goldfield is the most important gold producers of the East Kunlun metallogenic belt. Gold mineralization in this region is enigmatic, primarily because of uncertainties as to the mineralization processes, and the nature and sources of ore-forming fluids. Here, we investigate the ore-forming fluids and processes through a comprehensive study of the texture and geochemistry (LA-(MC)-ICPMS trace element analysis, mapping, S isotopes, and He-Ar isotopes) of pyrite from the Guoluolongwa gold deposit, the largest deposit in the Gouli goldfield. Four types of pyrite with distinct textures, trace element contents and sulfur isotopes were identified, and provide evidence for a multi-stage hydrothermal fluid evolution. The sedimentary-diagenetic Py0, representing the pre-ore stage, is characterized by high contents of Co and Ni, and negative $\delta^{34}S$ values (−11.6‰ to −4.0‰), which are notably different from the subsequent hydrothermal Py1 to Py3. Hydrothermal Py1, comprising subtypes Py1a and Py1b, was deposited in pyrite-quartz veins during stage I. The Py1a subtype shows characteristic Co-Ni-As oscillatory zoning that replaced Py0 via dissolution-reprecipitation, and hence inherited high concentrations of Co and Ni from Py0. In contrast, the Py1b subtype was devoid of Py0 influence and represented the initial ore-forming fluid with low concentrations of Co and Ni, moderate Cu, Pb, Zn, Sb, and Bi, but high As, Au, and Ag. The next stage, Py2, formed in the quartz-pyrite veins during stage II and showed clear textural and compositional contrasts to Py1. Specifically, Py2 has elevated Cu, Pb, Zn, Ag, and Bi contents and somewhat lower $\delta^{34}S$ values (+1.5‰ to +3.2‰) compared to Py1 (+1.6‰ to +5.6‰). In addition, Py2 shows irregular compositional zones, which we attribute to fluid phase separation caused by pressure fluctuation. Abundant Py2 precipitation triggered native gold deposition due to desulfidation of the ore-forming fluid. The next stage, Py3 in polymetallic sulfides-calcite-quartz veins at stage III, implies a new pulse of Cu-Pb-Zn-As-Au-Ag-rich and Bi-poor ore-forming fluid. This latter pyrite is characterized by inclusion-rich cores (Py3c), which contain abundant inclusions of chalcopyrite, galena, sphalerite, and native gold, and inclusion-free rims (Py3r). The cores, Py3c, likely represent abrupt destabilization of metal complexes and rapid precipitation during vigorous phase separation, whereas the euhedral Py3r rims formed under steadier physico-chemical conditions, contributing to lower $\delta^{34}S$ values of Py3c (+0.5‰ to +3.0‰) than Py3r (+1.9‰ to +3.6‰). Noble gas isotopes of Py1-Py3 have crust-dominated $^{3}He/^{4}He$ (0.04–0.4 Ra) and $^{40}Ar/^{36}Ar$ (623–2081), mixed with minor mantle components. Sulfur isotopes and low Co and Ni contents of hydrothermal pyrite, and He-Ar isotopes of fluid inclusions in pyrite, are consistent with a model in which multiple pulses of ore-forming fluids were exsolved during sequential episodes of primarily crustal-derived felsic magmatism with lesser mantle influences. This model is also supported by previous H-O isotope analyses, as well as widespread granitoid magmatism in the eastern Central East Kunlun Belt.

* Corresponding author at: Key Laboratory of Mineral Resources, Institute of Geology and Geophysics, Chinese Academy of Sciences, Beijing 100029, China.
*E-mail address:* fanhr@mail.iggcas.ac.cn (H.-R. Fan).

https://doi.org/10.1016/j.oregeorev.2021.104260
Received 25 March 2021; Received in revised form 18 May 2021; Accepted 24 May 2021
Available online 26 May 2021

## 1. Introduction

Orogenic gold deposits are amongst the most important sources of gold worldwide, accounting for nearly one third of resources (Large et al., 2011; Weatherley and Henley, 2013; Groves and Santosh, 2020). In terms of timing of formation, the orogenic gold deposits show several prominent episodes of peak formation during the late Archean to Paleoproterozoic and in Phanerozoic orogenic belts (Groves et al., 1998; Goldfarb et al., 2001; Tomkins, 2013). These deposits have been widely recognized to be temporally and spatially related to greenschist- to amphibolite-facies metamorphic and/or magmatic rocks (Groves et al., 1998; Phillips and Powell, 2009; Goldfarb and Groves, 2015). Two plausible sources of ore-forming fluids and metals have been proposed and debated for decades: namely, metamorphic devolatilization of volcano-sedimentary rocks, and exsolution from coeval intrusive magmas (Groves et al., 2016, 2020; Ridley and Diamond, 2000; Goldfarb et al., 2001; Phillips and Powell, 2009; Tomkins, 2013; Patten et al., 2020). In these deposits, as well as in porphyry, epithermal and carlin-type gold deposits, gold is commonly intimately related to iron-sulfide minerals such as pyrrhotite and pyrite, and the microstructures of these latter minerals are usually complex and compositions of trace elements and sulfur isotopes are representative in individual ore-forming stages (Large et al., 2009; Barker et al., 2009; Deditius et al., 2014; Peterson and Mavrogenes, 2014; Tanner et al., 2016). *In-situ* micro-analysis of pyrite allows us to determine textural and compositional features, and to investigate the chemical and isotopic evolution of the ore-forming fluids (Peterson and Mavrogenes, 2014; Chen et al., 2015; Li et al., 2018). Helium and Ar isotopes of fluids entrapped in pyrite are also powerful tools to fingerprint sources of ore-forming fluids (Burnard et al., 1999; Tan et al., 2018).

The East Kunlun Orogen (EKO) is an important poly-metallogenic belt, and records two stages of orogenesis that correspond to the evolution of the Neoproterozoic-Late Paleozoic Proto-Tethys Ocean and Late Paleozoic-Triassic Paleo-Tethys Ocean in this area (Yang et al., 1996; Chen et al., 2001; Dong et al., 2018). A number of gold deposits in this belt, represented by the Wulonggou (>70 t Au; Zhang et al., 2017) and Gouli (>110 t Au; Chen et al., 2020a) goldfields, have been discovered since the last decades. These deposits are characterized by structurally controlled quartz-sulfide vein-type or fracture-hosted pervasive alteration-type mineralization, which share similar features to the orogenic gold deposits (Groves et al., 1998; Feng, 2002; Zhao, 2004; Zhang et al., 2017; Chen et al., 2020a). Previous geochronological studies, such as sericite/muscovite Ar-Ar dating, have suggested that these deposits formed predominantly during the Triassic (Zhang et al., 2005, 2017; Xiao et al., 2014). However, recent studies have argued for at least two epochs of gold mineralization in the EKO, with ages of Devonian-Early Carboniferous and Late Triassic, based on pyrite Re-Os dating (Chen et al., 2020a). The ambiguity of the timing, and occurrence of two-episode or multi-stage mineralization events within a single region, make the mineralization processes enigmatic. Uncertainties regarding the mineralization processes and fluid sources hamper our understanding of the genesis of gold deposits in the EKO.

Previous studies have focused mainly on conventional bulk ore isotopes, fluid inclusions and geochronology (e.g., Li, 2017; Zhang et al., 2017; Chen, 2018; Chen et al., 2020a). In terms of the origin of ore-forming fluids in the EKO, some authors have suggested a relationship to contemporaneous magmatism (Zhang et al., 2017; Chen et al., 2020a), whereas others stress mixing of metamorphic and magmatic fluids with a late-stage input of meteoric water (Zou et al., 2011; Ding et al., 2013), or deep circulation of meteoric water (Feng, 2002). Here we addressed this unsettled question by detailed analyses of pyrite in Guoluolongwa deposit in the Gouli goldfield.

The Guoluolongwa gold deposit is the largest and representative deposit in the Gouli goldfield. Gold mineralization in the Guoluolongwa gold deposit is characterized by multi-stage quartz-sulfide veins containing abundant invisible and native gold. Pyrite grains with distinct occurrence are widespread in both host rocks and quartz-sulfide veins, and provide an opportunity to characterize the mineralization processes, properties, evolution and sources of ore-forming fluids. We studied pyrite from the Guoluolongwa gold deposit using a combination of microscopy, laser ablation inductively coupled plasma mass spectrometry (LA-ICPMS) for trace elements as well as elemental mapping, multi-collector laser ablation inductively coupled plasma mass spectrometry (LA-MC-ICPMS) for sulfur isotope analysis, and backscattered electron (BSE) scanning microscopy. Helium-Ar isotopic analysis on fluid inclusions in pyrite was conducted to constrain the source of ore-forming fluids. Our results provide insight into the gold precipitation, the composition, evolution, and source of ore-forming fluids in the Guoluolongwa gold deposit, further demonstrate a link between multi-stage hydrothermal events and sequential episodes of crust-derived magmas, with implications for gold metallogeny in the EKO.

## 2. Geologic background

The East Kunlun Orogen, comprising the western part of the Central Orogenic Belt of China (Fig. 1a), is located in the northern margin of the Tibetan Plateau, and is bounded by the Qaidam Basin to the north, the Bayan Har Terrane to the south, the NE-trending Altyn Tagh fault to the west, and the Qinling orogen to the east (Jiang et al., 2000; Xia et al., 2015). It can be divided into three tectonic belts, including the Northern Qimantagh Belt (NQB), the Central East Kunlun Belt (CEKB), and the Southern East Kunlun Belt (SEKB), which are separated by the Qimantagh-Xiangride ophiolitic mélange zone (QXM), the Aqikekulehu-Kunzhong ophiolitic mélange zone (AKM), and the Muztagh-Buqingshan-Anemaqen ophiolitic mélange zone (MBAM), from north to south (Fig. 1b) (Jiang et al., 1992, 2000; Dong et al., 2018). The NQB and QXM were correlated to the Qimantagh back-arc basin during Early Paleozoic northward subduction of the Proto-Tethys Ocean. The CEKB was an Early Paleozoic island-arc and Late Paleozoic-Triassic active continental marginal arc, while the AKM, MBAM, SEKB represent a wide and long-lived subduction and accretionary complex (Dong et al., 2018). These tectonic belts and ophiolitic mélange zones correspond to the evolution of the Proto-Tethys Ocean (Proterozoic-Early Paleozoic) and the Paleo-Tethys Ocean (Late Paleozoic-Mesozoic), mainly recorded by voluminous ophiolites with ages of ca. 537–436 Ma and ca. 345–243 Ma (Yang et al., 1996; Chen et al., 2001; Dong et al., 2018).

The basement in the EKO is dominated by Proterozoic granitic gneiss, amphibolite, and migmatites with minor granitoids, which crop out in all the three belts and are overlain by Paleozoic low-grade metamorphosed sedimentary and volcanic rocks (Jiang et al., 1992; Chen et al., 2013; Meng et al., 2013; Huang et al., 2014). The granitic gneiss has a peak magmatic age of ca. 920 Ma and a metamorphic age of 500–400 Ma (Chen et al., 2007). Some Mesozoic-Cenozoic sedimentary and volcanic rocks occur in the SEKB. Early Paleozoic-Mesozoic magmatic rocks are widespread in the EKO, mainly consisting of granitoids of two episodes during 466–390 Ma and 257–200 Ma (Mo et al., 2007; Huang et al., 2014; Shao et al., 2017; Dong et al., 2018; Zhao et al., 2020). Granitoids of both age groups show evolution from early calc-alkaline granodiorites to late monzogranites and syenogranites (Zhang et al., 2014; Chen et al.,2020b), and have been interpreted to be related to the subduction of the Proto-Tethys and Paleo-Tethys Oceanic Plate (Yin and Harrison, 2000; Mo et al., 2007; Chen et al., 2017). Minor mafic–ultramafic rocks occur along the CEKB with Cambrian-Ordovician ages of 537–467 Ma (Bian et al., 2004), and SEKB with both Cambrian-Ordovician (555–516 Ma; Liu et al., 2011) and Carboniferous ages (345–332 Ma; Chen et al., 2001; Liu et al., 2011).

The Gouli goldfield is located at the eastern end of the EKO, traversed by the NWW-trending AKM (Fig. 1b). The Paleoproterozoic Jinshuikou Group, which consists of gneiss, amphibolite, and marble, occurs throughout this region, and was unconformably overlain by the Ordovician-Silurian Naij Tai Group, the Devonian Maoniushan Formation, and Carboniferous-Triassic sedimentary and volcanic rocks.

Permian to Triassic granites and intermediate-felsic volcanic rocks are widespread in this area (Fig. 1c), including quartz diorite, granodiorite, monzogranite, andesite, and rhyolite. The Gouli batholith is part of this latter intermediate-felsic magmatic episode (Chen et al., 2017; Zhao et al., 2020). Some mafic dykes, such as the Annage gabbro, intrude the Paleoproterozoic basement and the Carboniferous to Triassic units (Zhao et al., 2019). A number of gold deposits in the Gouli goldfield have been recently discovered (Fig. 1c), including Guoluolongwa (>40 t Au), Walega (>12 t Au), Annage (>8 t Au), and Asiha (>6 t Au) (Chen et al., 2020a). These gold deposits are hosted within a variety of lithologies. The Annage and Guoluolongwa deposits are hosted in Proterozoic and early Paleozoic metamorphic rocks, respectively, and are mainly controlled by EW-trending brittle-ductile shear zones (Chen, 2018; Chen et al., 2020a). The Walega and Asiha deposits, which are controlled by NW- or NE-trending brittle fractures, are hosted in Silurian and Triassic granites, respectively (Chen et al., 2020a). Quartz-sulfide vein-type mineralization accounts for most of the gold resources in the Gouli goldfield, associated with lesser disseminated sulfide replacement and stockworks.

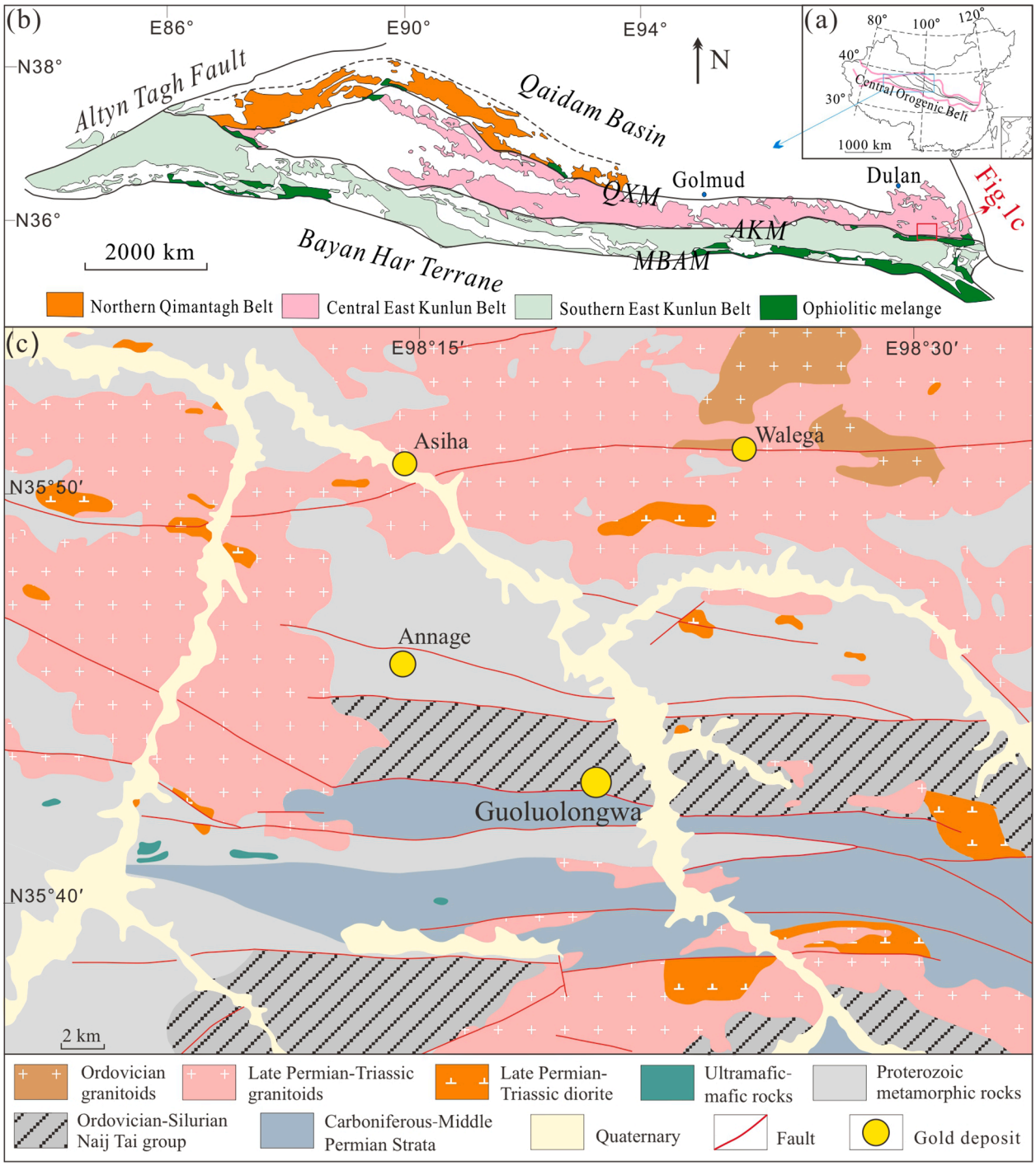


**Fig. 1.** (**a**) Tectonic map of China showing the location of the Central Orogenic Belt, and (**b**) Structural sketch of the East Kunlun Orogen, after Dong et al. (2018). (**c**) Geological map of the Gouli goldfield showing the distribution of gold deposits, after Chen et al. (2020a).

## 3. Deposit Geology

The Guoluolongwa gold deposit is located in the central part of the Gouli goldfield, and is the largest gold deposit in this area. The rock units around the deposit include Proterozoic schist to the north, Ordovician-Silurian Naij Tal Group metamorphic rocks in the center, Devonian conglomerates and Carboniferous-Middle Permian sedimentary-volcanic rocks to the south, and Ordovician-Silurian and Triassic magmatic rocks (Fig. 1c; Chen et al., 2020a). Gold mineralization at Guoluolongwa is predominantly hosted in quartz-sulfide veins. Six auriferous orebodies (I-VI) have been identified in the deposit, and are mainly hosted by phyllite from the Ordovician-Silurian Naij Tal Group (Fig. 2). Chen et al. (2020a) reported a metamorphic age of ca. 479 Ma for the Naij Tal Group, and suggested that the sedimentary and volcanic protoliths were formed no later than 479 Ma. The orebodies commonly occur as EW-striking, lenticular quartz-sulfide veins that are structurally controlled by the EW-trending thrust fault that formed in Silurian-Devonian (Wang et al., 2003). The veins dip steeply (45–75°) towards the south (170–180°), with variable lengths of 40–1340 m and thickness of 0.5–2.0 m. Average gold grades in the orebodies are 6.8 g/t with individual assay of up to 274.0 g/t where visible gold is present.

Each main orebody comprises a proximal alteration zone surrounding the auriferous quartz-sulfide veins (Fig. 3). Silicification, sericitization, pyritization, and carbonation occurred in the alteration zones, which were associated with strong foliation. The inner auriferous quartz-sulfide veins generally enclose lenticular clast or laminations of altered rocks (Fig. 3b, f, and g), suggesting progressive shear during mineralization (Davis and Hippertt, 1998). Besides gold, the major vein minerals include the sulfides pyrite, chalcopyrite, galena, and sphalerite, and the gangue minerals quartz, sericite, calcite, and siderite (Fig. 4).

One pre-ore (stage 0) and three ore stages (stages I, II, III) have been defined at Guoluolongwa gold deposit based on mineral assemblages and crosscutting relationships between veins and mineral textures within them (Fig. 3). The pre-ore stage is characterized by pyrite veinlets or disseminated euhedral pyrite grains/aggregates in the host phyllite (Fig. 3a and f). A majority of pyrite veinlets are sub-parallel to lithological layers or cleavage of the phyllite (Fig. 3e), and show evidence of shear deformation. Stage I is characterized by coarse-grained milky quartz veins with sparsely disseminated, coarse-grained pyrite. These stage I veins also commonly contain laminated fragments of host rock that commonly host fine-grained pyrite and lesser chalcopyrite (Fig. 3b, g, and j). Stage I veins are weakly gold mineralized. Some host-rock fragments within the stage I quartz veins show well-developed deformation cleavage as well as pre-ore pyrite veinlets (Fig. 3f). The milky quartz veins were cross-cut by massive quartz-pyrite veins in the second stage (stage II) and calcite-quartz-sulfide veins in the third stage (stage III, Fig. 3b and d). In contrast to stage I, the mineral assemblage in stage II veins consist of more pyrite, which commonly occurs as coarse-grained and massive clusters (Fig. 3c, h, and k), coexisting with calcite and quartz, as well as lesser chalcopyrite. Quartz veins of stage II are usually friable and porous. Stage III veins are composed of coarse-grained quartz, calcite, pyrite, chalcopyrite, sphalerite, and galena (Fig. 3i and l). Pyrite grains in this stage display intimate coprecipitation with chalcopyrite, galena, and sphalerite (Fig. 3i). The classification of ore stages is reasonably consistent with previous studies by Chen (2018) and Chen et al. (2020a). High-grade gold mineralization is associated with veins of both stages II and III. Native gold grains occur either along grain boundaries, within fractures or as inclusions entrapped within quartz and pyrite in all the three stages (Fig. 5). The most intense Au precipitation is concentrated in stage III, where irregular gold grains display an intimate paragenetic association with galena, sphalerite, and chalcopyrite (Fig. 5d and e).

## 4. Sampling and analytical methods

Petrographic studies were carried out on representative samples that were sampled from the underground tunnel of orebodies I and VI. Pyrite grains from all four stages (0, I, II, and III) were selected for *in-situ* textural and geochemical analyses, using field emission scanning electron micro-scope (FESEM), LA-ICPMS, and LA-MC-ICPMS, and were separated for noble gases analyses.

### 4.1. Field emission scanning electron microscope

Microstructural analysis of the mineral phase was performed using a Nova NanoSEM 450 FESEM equipped with an X-MAXN80 Energy Dispersive X-ray Spectrometer (EDS), at the Institute of Geology and Geophysics, Chinese Academy of Sciences (IGGCAS). Backscattered electron images were acquired at an accelerating voltage of 15 kV and a primary beam current of 20nA.

### 4.2. In-situ trace element analysis and mapping of pyrite

Trace elements in pyrite were measured on an Agilent 7900 ICP-MS instrument attached to a Geolas HD laser ablation system (LA-ICPMS), at the Wuhan Sample Solution Analytical Technology Co., Ltd., China. A "wire" signal smoothing device was included in the laser ablation system (Hu et al., 2015). The spot size and frequency of the laser were set to 32

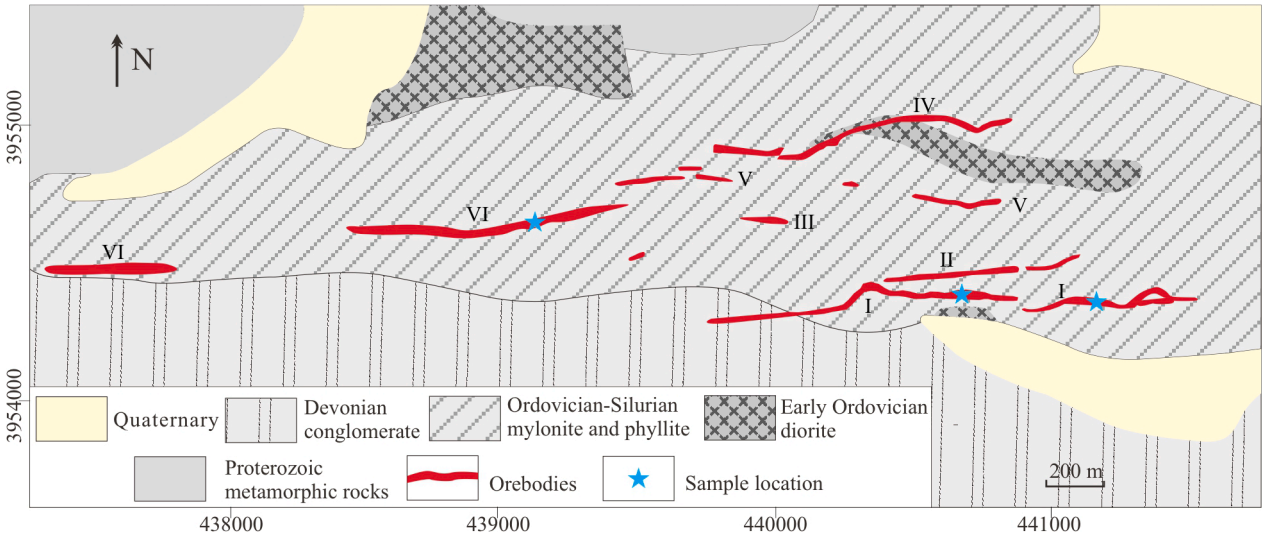


**Fig. 2.** Geological map of the Guoluolongwa gold deposit showing the distribution of the orebodies, after Chen et al. (2020a).

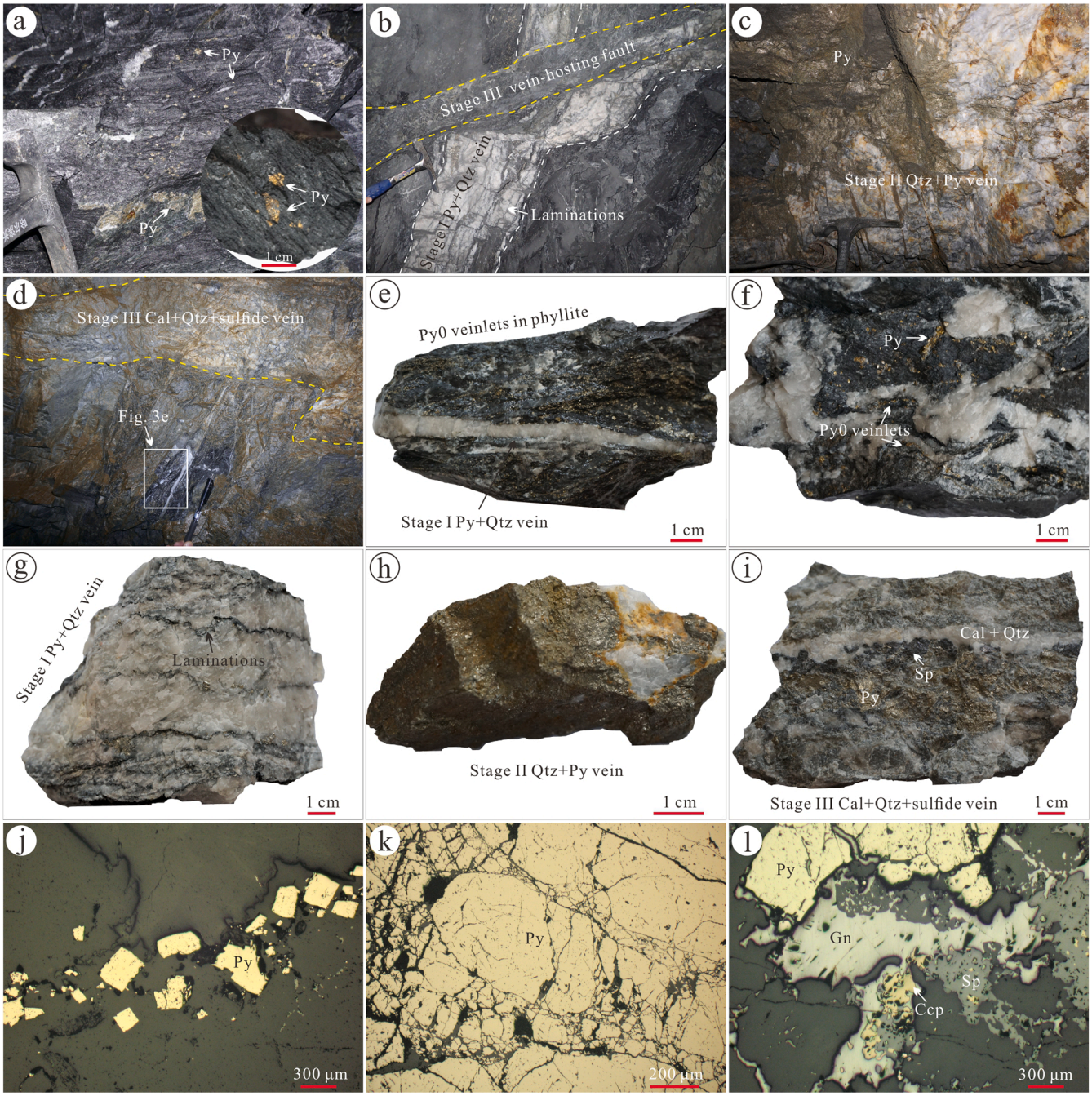


**Fig. 3.** Photographs and reflected light images of ore veins, hand specimens, and mineral assemblages in distinct stages. (**a, e, f**) Pre-ore-stage disseminated pyrite and pyrite veinlets in the host phyllite, cut by stage-I milky quartz veins. (**b, g, j**) Pyrite-milky quartz veins in stage I, with laminations of host-rock materials and fine-grained pyrite, cut by later veins. (**c, h, k**) Quartz-pyrite veins in stage II with abundant coarse-grained pyrite clusters. (**d, i, l**) Calcite-quartz-pyrite-chalcopyrite-sphalerite-galena veins in stage III. *Qtz* quartz, *Cal* calcite, *Py* pyrite, *Ccp* chalcopyrite, *Sp* sphalerite, *Gn* galena.

μm and 5 Hz, respectively. The sulfide reference material MASS-1 (USGS) was used as an external bracketing standard. The data quality was monitored by analyzing the NIST 610 reference glass and the MASS-1 as unknowns interspersed with the measurements of the samples. Each analysis incorporated a background acquisition of approximately 20–30 s followed by 50 s of data acquisition. An Excel-based software ICPMSDataCal was used to perform off-line selection and integration of background and analyzed signals, drift correction, and quantitative calibration for trace element analysis (Liu et al., 2008). Details of the operating conditions and data reduction followed that description by Liu et al. (2008).

Trace element mapping of pyrite was performed by a set of parallel lines of ablation using an Agilent 7700x ICP-MS equipped with a Coherent Compex-Pro 193 nm ArF excimer laser at the State Key Laboratory of Ore Deposit Geochemistry, Institute of Geochemistry, Chinese Academy of Sciences. The line ablations were carried out using a beam size of 7 μm with a repetition rate of 10 Hz and a rastering speed of 7 μm/s. The isotopes selected for image analysis were: $^{56}$Fe, $^{59}$Co, $^{60}$Ni, $^{65}$Cu, $^{66}$Zn, $^{75}$As, $^{77}$Se, $^{109}$Ag, $^{121}$Sb, $^{197}$Au, $^{208}$Pb and $^{209}$Bi. Acquisition time was set to 0.002 s for most elements, except Au and Ag (0.004 s each), and the total sweep time was ~0.2 s. The complete maps were generated over a period of approximately 2–3 h each, to keep instrument drift in sensitivity to the minimum. The standards STDGL3, GSE-1G, and GSD-1G were used to calibrate the concentrations of trace elements and to

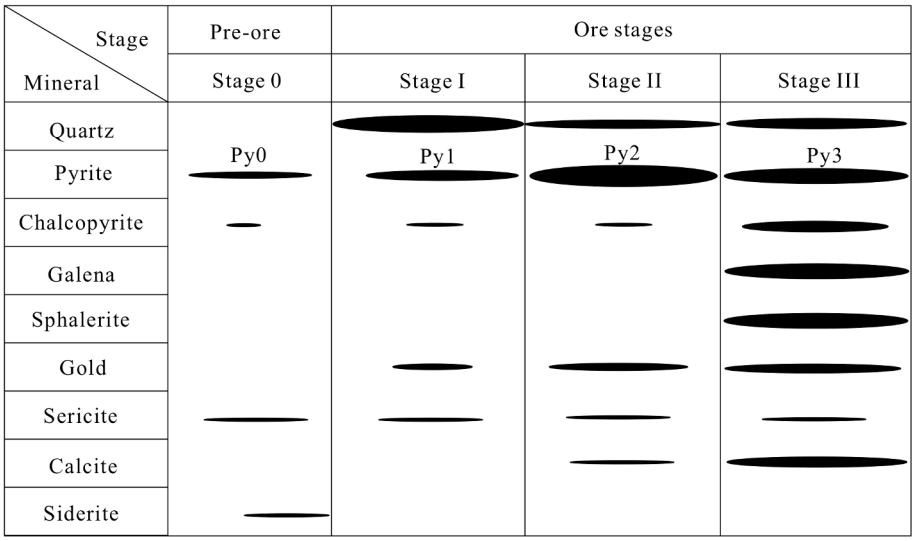


**Fig. 4.** Mineral paragenetic sequence of the Guoluolongwa gold deposit.

monitor the drift in sensitivity (Danyushevsky et al., 2011).

### 4.3. In-situ s isotope analysis of pyrite

*In-situ* sulfur isotopes of pyrite were analyzed by LA-MC-ICPMS at the Wuhan Sample Solution Analytical Technology Co., Ltd, China. A Neptune Plus MC-ICPMS instrument equipped with a Geolas HD excimer ArF laser ablation system was used. In the laser ablation system, helium was used as carrier gas for the ablation cell and was mixed with argon (makeup gas) after the ablation cell. Pyrite was ablated at a large spot size (44 μm) and slow pulse frequency (2 Hz) to avoid the down-hole fractionation effect which has been reported by Fu et al. (2016), with the laser fluence kept constant at 5 J/cm$^2$. Isotopes $^{32}$S, $^{33}$S, and $^{34}$S were collected in Faraday cups using static mode. Each analysis incorporated 20 s baseline time, 40 s ablation time, and 40 s wash time. A standard-sample bracketing method with three samples bracketed by a pyrite pressed powder tablet was employed to correct for instrumental mass fractionation. Pyrite standard PPP-1 (Gilbert et al., 2014) was used as a reference material to avoid the matrix effect (Fu et al., 2016). The in-house reference pyrite SP-Py-01 ($\delta^{34}S_{VCDT}$ = 2.0‰ ± 0.5‰) was analyzed repeatedly as an unknown sample to verify the accuracy of the calibration method. Standard errors for PPP-1 and SP-Py-01 are ± 0.1‰ (2σ; N = 48) and ±0.3‰ (2σ; N = 16), respectively.

### 4.4. Helium-Ar isotopic analysis

Pyrite crystals for noble-gas isotope analysis were crushed into 20–40 mesh, and were handpicked under a binocular microscope (>99% purity). After ultrasonic washing and drying, each sample was loaded into the crushing chamber and then baked under vacuum for three days to avoid any adsorbed atmospheric gases. Helium and Ar isotopes were measured using the Nu Instruments Noblesse mass spectrometer at IGGCAS. The detailed operating and data processing procedures were described by He et al. (2011). Noble gases were extracted from the pyrite by a one-step or multi-step crushing process in a vacuum crusher at 20000-psi pressure. The Ar in the noble gas mixtures was trapped in a cold finger with charcoal at the temperature of liquid nitrogen. Helium was trapped in cold finger at about 13 K and released at 35 K. Helium and Ar were introduced separately into the mass spectrometer and analyzed in static mode. Line blanks were run before each measurement, producing negligible He blanks ($^3$He < 3 × 10$^{-17}$ cc STP) and low Ar blanks ($^{40}$Ar < 4 × 10$^{-11}$ cc STP), about 0.1% of the signal from samples. The data were corrected for system blank and further calibrated by air shot and Helium HESJ standards (He Standard of Japan; $^3$He/$^4$He = 20.63 ± 0.10 Ra; Matsuda et al., 2002).

## 5. Results

### 5.1. Classification and textures of pyrite

Pyrite is the dominant repository of gold in the Guoluolongwa quartz-sulfide veins, but gold is only present in certain pyrite types. Thus, it is critical to classify and differentiate the different types of pyrite. Based on petrographic characteristics, BSE observation, and geochemical analyses of pyrite in both barren host rocks and high-grade orebodies, four types of pyrite were recognized in the Guoluolongwa gold deposit. The key textural characteristics of individual pyrite types are described below in paragenetic order.

The first generation of pyrite (Py0) is predominantly found in the host phyllite (Fig. 3a, e, and f), occurring as either disseminated single grains/aggregates or small veinlets. The disseminated Py0 grains are characterized by euhedral-subhedral shape and abundant, randomly oriented silicate-carbonate inclusions (Fig. 6a and d), as well as lesser micro-inclusions of chalcopyrite. Some Py0 grains are composed of an inclusion-rich core and a thin, inclusion-poor rim (Fig. 6d). The Py0 veinlets are aligned as interlayers in deformation cleavage of the host phyllite (Fig. 3e), or developed around segregation quartz veins that formed during metamorphism. In the veinlets, coarse euhedral Py0 grains were broken down into small fragments and retained breakdown textures along their rims (Fig. 6b and e). The fragments were cemented by interstitial siderite (Fig. 6b and e).

The second generation of pyrite (Py1), with rare or no mineral inclusions, can be split into sub-types according to occurrence. The first sub-type (Py1a) occurs as thick overgrowths on the inclusion-rich and corroded crystals of Py0 (Fig. 6g and h). The second sub-type (Py1b) is commonly present as single grains or along irregular laminae in quartz veins of stage I (Fig. 6c and f). Py1a grains are found in pyrite veinlets that occur as interlayers in the phyllite (Fig. 6h). The host phyllite, as well as pyrite (Py0 + Py1a) veinlets, was laminated or cut by milky quartz veins in stage I (Fig. 3e, f, and g), suggesting that the precipitation of Py1a was earlier than or nearly simultaneous with formation of the stage I milky quartz. The Py1 is typically euhedral and fine grained. The volumetric proportion of Py1 relative to quartz is low in stage I. In backscattered electron (BSE) images, Py1 grains show no detectable zoning (Fig. 6f, g, and h), suggesting a relatively homogeneous composition.

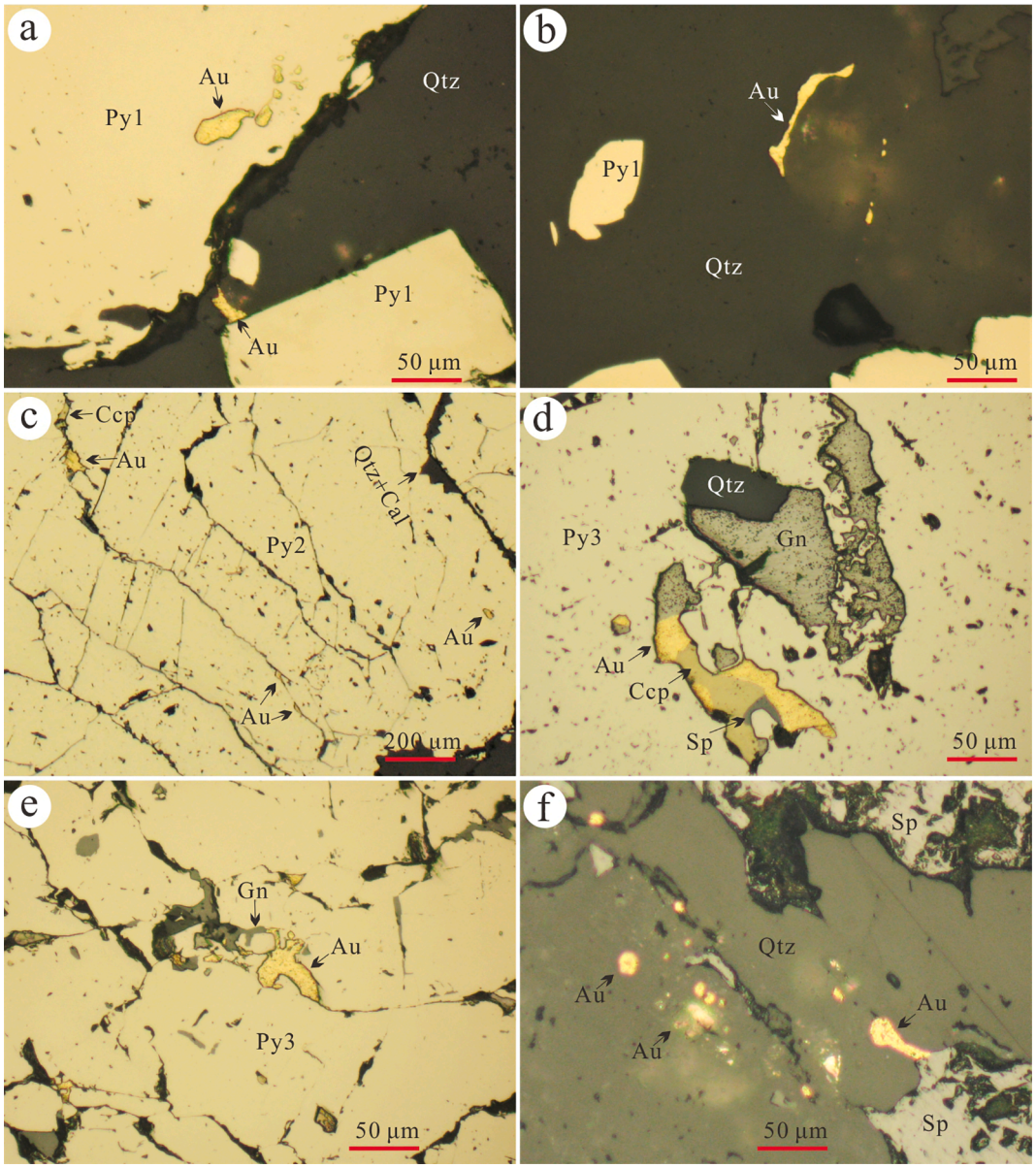


**Fig. 5.** Reflected light images showing the distribution of native gold grains, (**a, b**) in Py1 and stage-I quartz veins, (**c**) occur as inclusions and fracture fill within Py2, (**d, e**) show intimate paragenetic association with galena, sphalerite, and chalcopyrite in stage III, (**f**) distribute in quartz in stage III. *Qtz* quartz, *Cal* calcite, *Py* pyrite, *Ccp* chalcopyrite, *Sp* sphalerite, *Gn* galena, *Au* gold.

Pyrite in stage II (Py2) is coarser grained than both Py0 and Py1, and occurs as subhedral to anhedral aggregates with minor chalcopyrite inclusions (Fig. 6i and j). The Py2 is either confined to quartz-pyrite veins as pyrite clusters, or forms massive pyrite veins adjacent to quartz veins. In the quartz-pyrite veins, the volumetric proportion of Py2 is high relative to quartz. Backscattered electron images of Py2 show significant compositional variation, distinct from Py1 (Fig. 6j). Fractures are commonly developed in Py2, and are commonly cemented by native gold, chalcopyrite, calcite, and quartz (Fig. 6i and j).

The fourth generation of pyrite, Py3, is present in stage III and coexists with chalcopyrite, sphalerite, galena, quartz, and calcite (Fig. 3l). Distinctively inclusion-rich cores, denoted Py3c, contain abundant chalcopyrite, galena, sphalerite, and gold inclusions, and are enveloped by euhedral, inclusion-free rims denoted Py3r (Fig. 6k, l). The Py3 occurs in a variety of habits, including compact euhedral-subhedral clusters, isolated anhedral coarse grains, and fine grains with euhedral morphologies. Native gold occurs as inclusions and fracture fill within Py3 and show an intimately paragenetic association with galena, chalcopyrite, and sphalerite (Fig. 5d, e).

### 5.2. Sulfur isotopic compositions of pyrite

The S isotopic compositions of four types of pyrite measured by LA-MC-ICPMS are presented in Supplementary Table 1 and Fig. 6. The data show a clear difference between the S isotopes of Py0 versus those of Py1through Py3. The $\delta^{34}S$ values of Py0 show a negative and wide range from −11.6‰ to −4.0‰, with 2/3 of the data falling between −11.6‰ to −10.6‰ (Fig. 7), the other 1/3 data ranging from −8.9‰ to −4.0‰. The other three types of pyrite have positive ranges of S isotopic compositions, extending from +0.5‰ to +5.6‰. In detail, each type of pyrite has a slightly different range of $\delta^{34}S$ values. The Py1 has the highest $\delta^{34}S$ values, ranging from +1.6‰ to +5.6‰ with an average value of + 3.6‰. The $\delta^{34}S$ values of the Py1a sub-type are +1.6‰ to +4.5‰ (average +3.3‰), and those of Py1b are +3.5‰ to +5.6‰ (average +4.9‰). In contrast, both Py2 and Py3 have lower ranges of $\delta^{34}S$ values of +1.5‰ to +3.2‰ (average + 2.2‰) and +0.5‰ to +3.6‰ (average

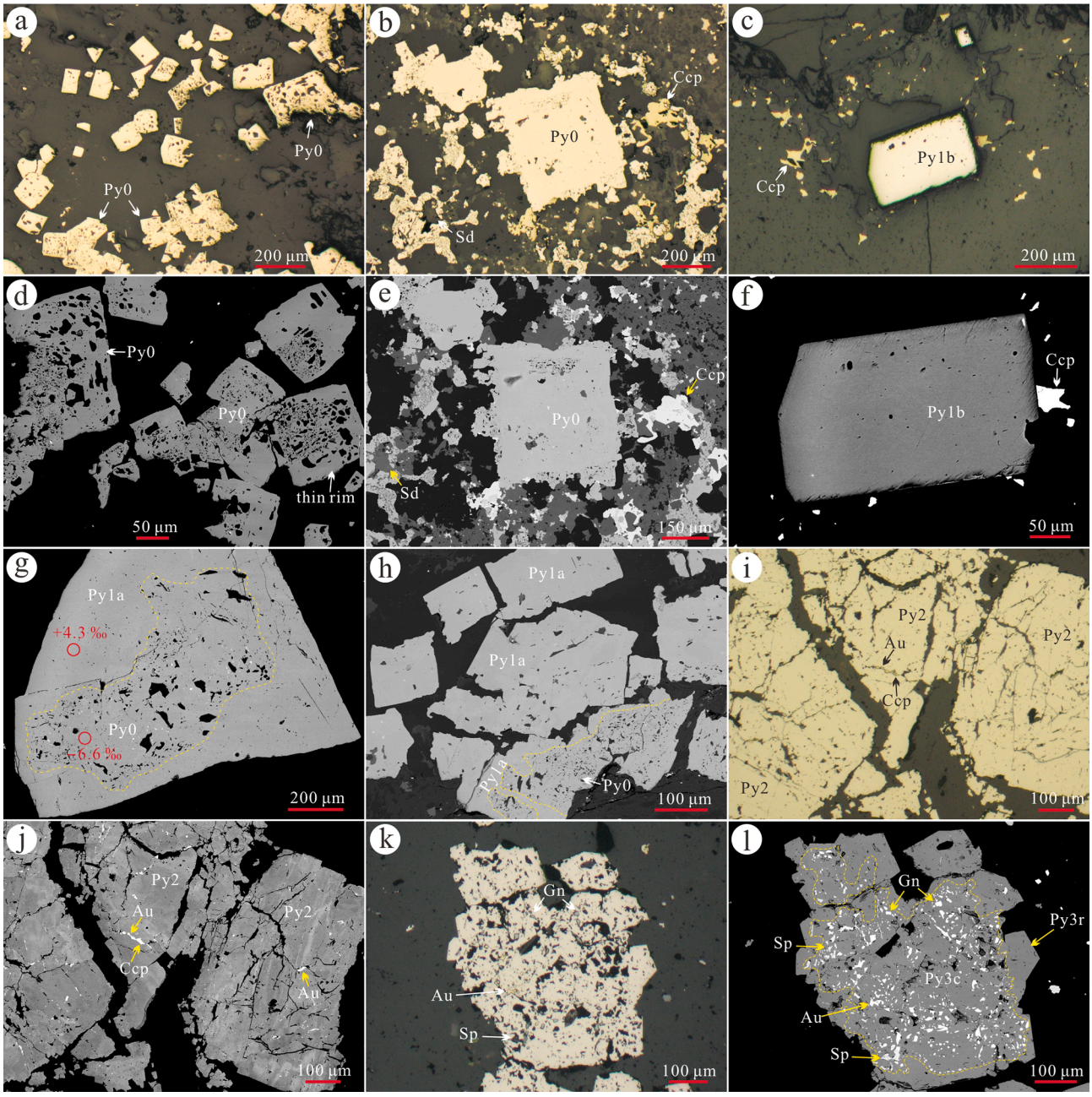


**Fig. 6.** Reflected light and BSE images of the four pyrite types. (**a, d**) Disseminated Py0 with abundant silicate-carbonate inclusions. (**b, e**) Py0 grains showing breakdown textures in veinlets. (**c, f, g, h**) Py1 grains, including Py1a as overgrowths on Py0, and euhedral independent Py1b. (**i, j**) Anhedral Py2 grains with irregular BSE compositional zoning. (**k, l**) Py3 is composed of an inclusion-rich core (Py3c) and an inclusion-free rim (Py3r). *Sd* siderite, *Py* pyrite, *Ccp* chalcopyrite, *Sp* sphalerite, *Gn* galena, *Au* gold.

**Table 1**
Helium and Ar isotopic compositions of fluid inclusions in pyrite from the Guoluolongwa gold deposit.

| Sample no. | Type | $^{4}$He ($E^{-7}$) | $^{3}$He/$^{4}$He (Ra) | σ | $^{40}$Ar ($E^{-7}$) | $^{40}$Ar* ($E^{-7}$) | $^{40}$Ar/$^{36}$Ar | σ | $^{40}$Ar*/$^{4}$He | $^{3}$He/$^{36}$Ar ($E^{-4}$) |
|---|---|---|---|---|---|---|---|---|---|---|
| 19GW14 | Py0 | 2.06 | 0.03 | 0.01 | 7.47 | 3.74 | 597 | 8 | 1.82 | 0.06 |
| 19GW44 | Py0 | 8.16 | 0.06 | 0.01 | 1.05 | 0.71 | 940 | 6 | 0.09 | 6.23 |
| 19GW19 | Py1 | 32.24 | 0.04 | 0.01 | 13.19 | 7.58 | 701 | 9 | 0.24 | 0.85 |
| 19GW29 | Py2 | 21.47 | 0.13 | 0.01 | 10.44 | 6.03 | 706 | 9 | 0.28 | 2.72 |
| 19GW36 | Py2 | 25.79 | 0.11 | 0.01 | 9.78 | 6.02 | 775 | 5 | 0.23 | 3.20 |
| 19GW03 | Py3 | 50.96 | 0.08 | 0.01 | 84.28 | 72.21 | 2081 | 27 | 1.42 | 1.42 |
| 19GW06 | Py3 | 12.05 | 0.18 | 0.01 | 7.67 | 4.00 | 623 | 8 | 0.33 | 2.44 |
| 19GW18 | Py3 | 15.66 | 0.40 | 0.03 | 16.39 | 11.18 | 936 | 12 | 0.71 | 4.92 |

*Note:* The unit for $^{4}$He, $^{40}$Ar and $^{40}$Ar* is ccSTP/g.

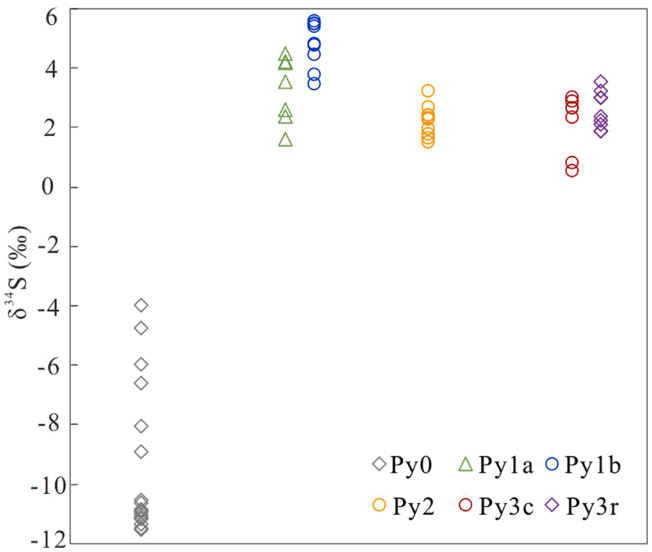


**Fig. 7.** *In-situ* sulfur isotopes of distinct types of pyrite from the Guoluolongwa gold deposit.

+ 2.4‰), respectively (Fig. 7).

At the scale of individual pyrite grains, some Py0 grains show an increasing trend of $\delta^{34}S$ values from the core (e.g., −10.9‰). For those grains consisting of Py0 cores and Py1a rims, as shown in Fig. 6g, the Py0 core has a $\delta^{34}S$ value of −6.6‰, whereas the Py1a rim has a $\delta^{34}S$ value of +4.3‰. Grain-scale variations in sulfur isotopes are also notable in Py3 grains that show core-rim textures. In sample 19GW03, cores of Py3c have low $\delta^{34}S$ values of +2.4‰ to +3.0‰, whereas Py3r rims shows slightly higher $\delta^{34}S$ values of +3.0‰ to +3.6‰ (Fig. 7; Supplementary Table 1). In sample 19GW18, two data points from inclusion-rich Py3c cores yield low $\delta^{34}S$ values of +0.5‰ and +0.8‰, whereas rims of Py3r show $\delta^{34}S$ values of +1.9‰ to +3.0‰ (Fig. 7; Supplementary Table 1).

### 5.3. Trace element compositions of pyrite

Trace elements of four types of pyrite analyzed by LA-ICPMS are listed in Supplementary Table 1 and displayed in Fig. 8. Evaluation of the data focused on trace elements with significant concentrations in the pyrite samples, such as Co, Ni, Cu, Zn, As, Ag, Sb, Au, Pb, and Bi. Among the investigated pyrite grains from the Guoluolongwa gold deposit, the inclusion-rich Py0 grains recorded the highest concentrations of Co (11.3–350.5 ppm, median 107.8 ppm) and Ni (15.9–1442.8 ppm, median 423.6 ppm), but low levels of other trace elements. Py0 grains are characterized by low Co/Ni ratios (0.03–1.4, 0.4 on average; Fig. 9c). Notably, Au contents of Py0 are consistently low and mostly below the limits of detection.

In Py1, Co (1.8–448.8 ppm, median 76.2 ppm) and Ni (0.3–522.6 ppm, median 136.4 ppm) concentrations are highly variable, similar to Py0, but higher than Py2 and Py3. It should be noted that the Py1 grains with relatively high Co and Ni concentrations are mostly Py1a sub-type that overgrew grain of earlier Py0. The Co/Ni ratios of Py1 range from 0.2 to 13.8 (2.3 on average; Fig. 9c), with one outlier showing a ratio of 444.2. Copper, Pb, Zn, Sb, and Bi contents in Py1 are low (Fig. 8), similar to those of Py0, excluding one data point with high Cu (58.8 ppm) and Zn (2080.2 ppm) concentrations due to micro-inclusions of chalcopyrite and sphalerite. Arsenic is enriched in Py1, ranging from 257.6 ppm to 2819.4 ppm with a median value of 618.3 ppm and an outlier of 3.2 ppm. The variation of As contents is systematically coupled with Au contents (Fig. 9d). Grains of Py1 also have slightly elevated Ag (0.0–12.2 ppm, median 0.2 ppm) and Au (0.004–1.76 ppm, median 0.09 ppm) concentrations compared to Py0.

The Py2 grains are rich in Cu (0.3–60.8 ppm, median 4.1 ppm), Zn (0.8–2678.6 ppm, median 5.7 ppm), As (0.5–1041.2 ppm, median 261.2 ppm), Ag (0.1–4.27 ppm, median 1.1 ppm), Sb (0.08–1.2 ppm, median 0.5 ppm), Au (0.02–0.3 ppm, median 0.06 ppm), Pb (3.4–62.2 ppm with an outlier of 722.1 ppm, median 21.1 ppm), and Bi (0.2–10.0 ppm, median 6.3 ppm), but poor in Co (0.0–9.0 ppm, median 0.7 ppm) and Ni (0.0–3.5 ppm, median 2.5 ppm) with Co/Ni ratios of 0.1 to 3.0 (1.2 on average; Fig. 9c). Specifically, Bi contents in Py2 reach the highest levels among all the samples. Some extremely high Zn values (1039.9–2678.6 ppm) and one anomalous Pb value (722.1 ppm) are probably attributed to micro-inclusions of sphalerite and galena, respectively. Gold contents in Py2 are similar to those of Py1 and higher than Py0.

Compared to Py2, the contents of most trace elements in Py3 are higher and show large variations, except for Bi (Fig. 8). For example, the Py3 grains have ranges of 0.1 to 118.7 ppm (median 6.9 ppm, with an outlier of 712.3) for Co and 0.0 to 90.7 ppm (median 4.2 ppm) for Ni, which are higher than those of Py2 but still lower than those of Py0 and Py1. The Co/Ni ratios of Py3 range widely from 0.2 to 28.5 (4.7 on average; Fig. 9c). Copper (0.0–54.8 ppm, median 2.0 ppm), Zn (0.7–56.6 ppm, median 3.0 ppm, with two outliers of 1050.8 ppm and 3575.6 ppm), As (0.0–4859.6 ppm, median 474.8 ppm), Ag (0.0–19.2

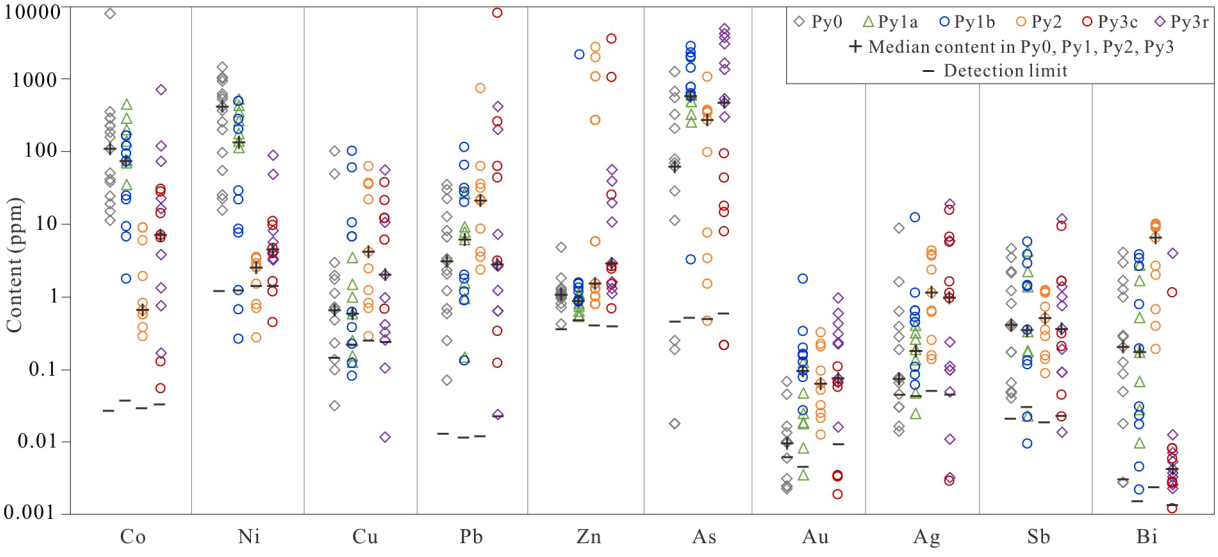


**Fig. 8.** Trace elements of distinct types of pyrite. Note that median contents for Py1 and Py3 are calculated based on the overall data.

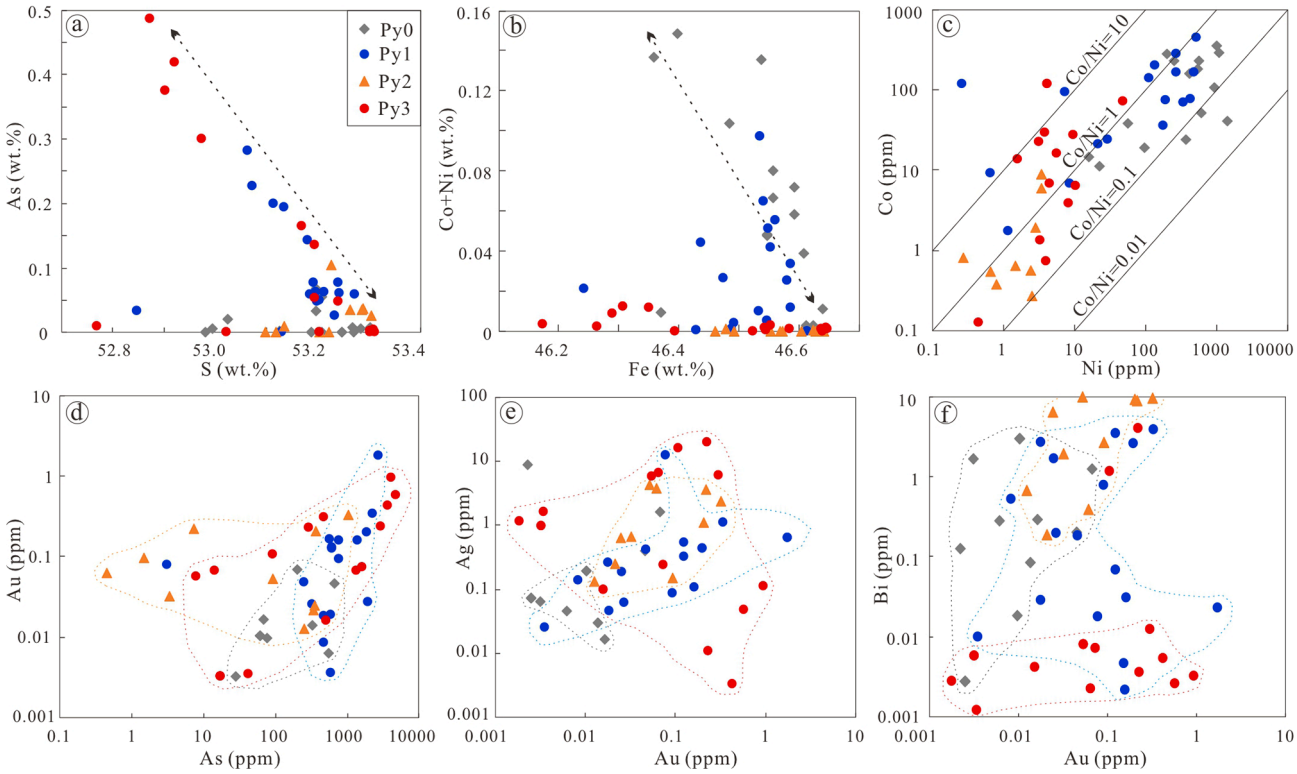


**Fig. 9.** Selected binary plots showing the geochemical characteristics of four types of pyrite. Plots of (**a**) As versus S, (**b**) Co + Ni versus Fe, (**c**) Co versus Ni, (**d**) Au versus As, (**e**) Ag versus Au, and (**f**) Bi versus Au.

ppm, median 0.97 ppm), Sb (0.01–11.7 ppm, median 0.4 ppm), Au (0.0–0.9 ppm, median 0.07 ppm), and Pb (0.0–419.3 ppm, median 2.8 ppm, with an outlier of 8536.4 ppm) in Py3 reach the highest concentrations amongst all of our analyses. However, the contents of Bi in Py3 are the lowest (Fig. 9f), ranging from 0.0 ppm to 4.0 ppm (median 0.004 ppm). The concentrations of As and Au in Py3 display a positive correlation (Fig. 9d). Significantly, the contents of Co, Ni, As, and Au in rims of Py3r are obviously higher than those of the corresponding Py3c cores, whereas other elements are indistinguishable between core and rim (Fig. 8). The abnormally high values of Zn (1050.8 ppm and 3575.6 ppm) and Pb (8536.4 ppm) in Py3c are attributed to inclusions of sphalerite and galena, consistent with our petrographic observations.

### 5.4. Trace elemental mapping of pyrite

Mapping by LA-ICPMS was conducted to study the distribution of trace elements on the grain scale. One representative grain comprising a Py0 core and Py1a rim is displayed in Fig. 10. The contact between core and rim is quite irregular, illustrated by the distribution of trace elements. The Py0 core has moderate Co, Ni, and As concentrations, whereas these elements are higher in the Py1a rim and show oscillatory zoning (Fig. 10). Some micro-inclusions of chalcopyrite are present in the Py0 core, evidenced by locally anomalous Cu values. The Py1a rim is effectively barren of Pb, Zn, Sb, Bi, and Se relative to the Py0 core. Additionally, the contents of Au and Ag are low in the whole grain, except for areas with high As contents in the Py1a rim (Fig. 10).

Trace elemental mapping was also conducted on a Py3 grain that shows a core of Py3c and a rim of Py3r (Fig. 11). The Py3c core shows high contents and systematic variation of Cu, Pb, Zn, Au, Ag, Sb, and Bi due to abundant micro-inclusions of chalcopyrite, galena, sphalerite, and gold. In contrast, the Py3r rim has lower contents of Cu, Pb, Zn, Ag, Sb, and Bi, but higher contents of Co, Ni, As, and Se. Except for the gold particles, Au contents in Py3r are slightly higher than Py3c (Fig. 11).

### 5.5. Helium-Ar isotopes of pyrite

The results of He and Ar isotope analyses of fluid inclusions in pyrite are listed in Table 1 and illustrated in Fig. 12. Two samples of Py0 from the host metamorphic rocks have low $^{4}He$ contents of $2.1 \times 10^{-7}$ ccSTP/g and $8.2 \times 10^{-7}$ ccSTP/g, low $^{3}He/^{4}He$ ratios of $0.03 \pm 0.01$ Ra and $0.06 \pm 0.01$ Ra (where Ra is the $^{3}He/^{4}He$ ratio of air $= 1.39 \times 10^{-6}$). Concentrations of $^{40}Ar$ from the two Py0 samples are $7.5 \times 10^{-7}$ ccSTP/g and $1.0 \times 10^{-7}$ ccSTP/g, with $^{40}Ar/^{36}Ar$ ratios of $597 \pm 8$ and $940 \pm 6$, and $^{40}Ar^{*}$ (where $^{40}Ar^{*}$ is the radiogenic $^{40}Ar$ present, corrected for atmospheric contributions assuming that all $^{36}Ar$ is atmospheric in origin and an atmospheric $^{40}Ar/^{36}Ar$ of 295.5; Burnard et al., 1999) are $3.7 \times 10^{-7}$ ccSTP/g and $0.7 \times 10^{-7}$ ccSTP/g. The calculated $^{40}Ar^{*}/^{4}He$ ratios are 1.8 and 0.1, and $^{3}He/^{36}Ar$ values are $0.06 \times 10^{-4}$ to $6.2 \times 10^{-4}$.

Six samples (including one of Py1, two of Py2, and three of Py3) from the orebodies have high $^{4}He$ contents ranging from $12.1 \times 10^{-7}$ ccSTP/g to $51.0 \times 10^{-7}$ ccSTP/g, low $^{3}He/^{4}He$ ratios of 0.04–0.40 Ra (average 0.16 Ra). The $^{40}Ar$ concentrations vary from $7.7 \times 10^{-7}$ ccSTP/g to $84.3 \times 10^{-7}$ ccSTP/g, and $^{40}Ar^{*}$ are between $4.0 \times 10^{-7}$ ccSTP/g and $72.2 \times 10^{-7}$ ccSTP/g. Ratios of $^{40}Ar/^{36}Ar$ are in the range of 623–2081, with an average of 970, and are higher than the air ratio and much lower than that of typical MORB mantle (30,000–40,000; Kendrick and Burnard, 2013). The $^{3}He/^{36}Ar$ values are from $0.76 \times 10^{-4}$ to $5.45 \times 10^{-4}$, the $^{40}Ar^{*}/^{4}He$ are between 0.2 and 1.4 (average 0.5), and the $^{3}He/^{36}Ar$ values range from $0.8 \times 10^{-4}$ to $4.9 \times 10^{-4}$. It should be noted that the result of Py1 is inevitably influenced by Py0 because of the overgrowth relationship.

## 6. Discussion

### 6.1. Evaluation of trace element signatures

Numerous studies have demonstrated that pyrite can effectively incorporate a wide array of trace metals in its structure, both in solid

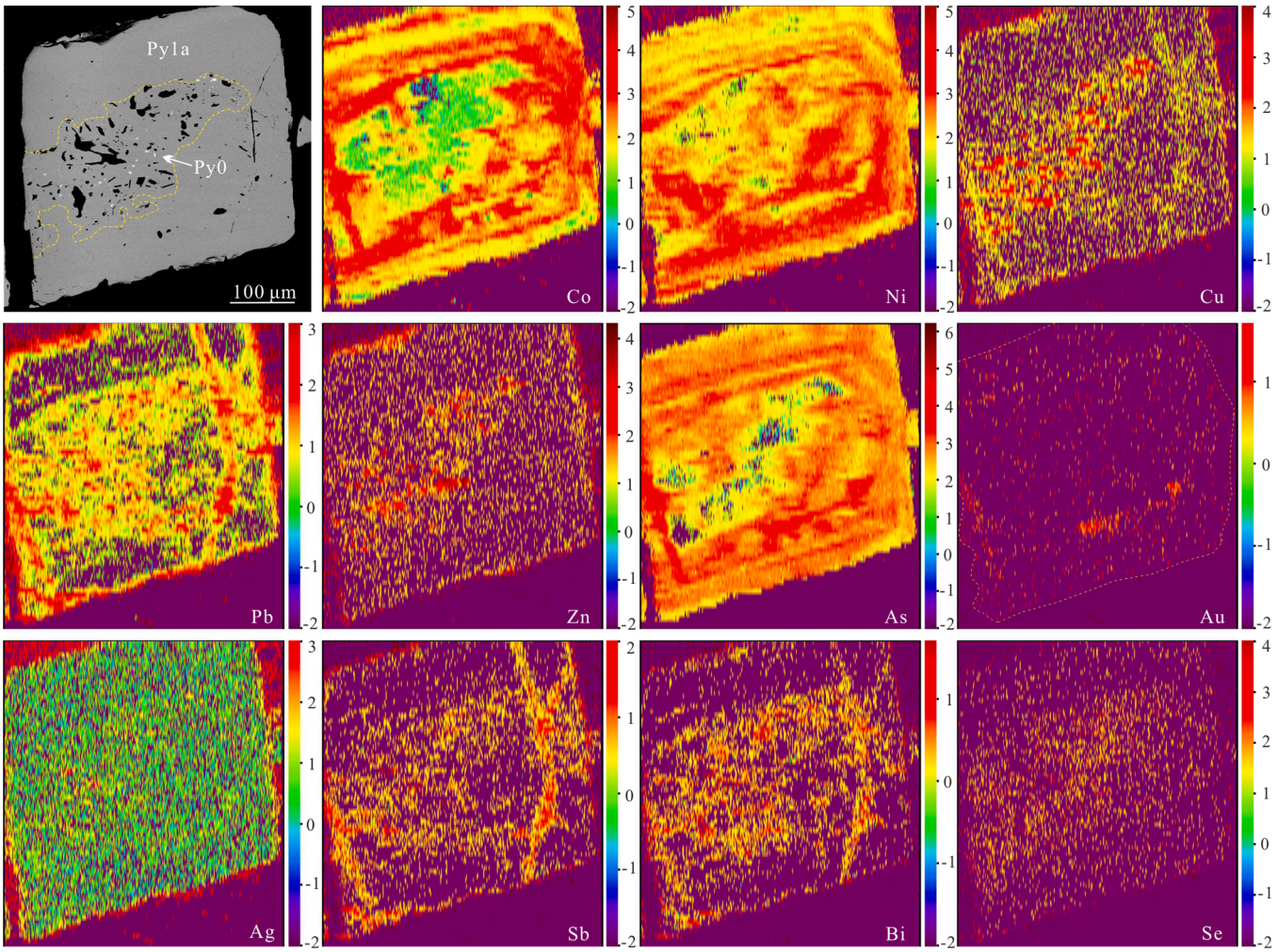


**Fig. 10.** LA-ICPMS trace elemental maps, and a BSE image, of pyrite with a Py0 core and a Py1a rim. Concentration scales are in ppm (logarithmic $10^n$, where n is given on scale).

solution and as nanoparticles, and therefore pyrite can serve as a metal scavenger and monitor for the changes in hydrothermal fluid composition (Reich et al., 2005; Large et al., 2009; Deditius et al., 2014; Tardani et al., 2017). Significant variations of Co, Ni, Cu, Pb, Zn, As, Au, Ag, Sb, and Bi are present among distinct generations of pyrite and within individual pyrite grains from the Guoluolongwa gold deposit (Supplementary Table 1; Figs. 8–11). The following discussion focuses on potential determinants on these variations. Elemental correlations for As-S, (Co + Ni)-Fe, Co-Ni, Au-As, Ag-Au, and Bi-Au pairs are shown in Fig. 9.

Both Co and Ni may substitute stoichiometrically for Fe in the octahedral site of pyrite, owing to the fact that $Co^{2+}$ and $Ni^{2+}$ have similar ionic radii to that of $Fe^{2+}$ (Abraitis et al., 2004; Reich et al., 2013). This substitution is supported by the Co and Ni concentrations reported here for Py0 and Py1, which show a negative correlation with Fe (Fig. 9b). The Co/Ni ratio in pyrite is sensitive to environmental change and has been widely used to classify the origin and source of hydrothermal mineral deposits (Bralia et al., 1979; Campbell and Ethier, 1984; Bajwah et al., 1987; Large et al., 2009). In general, sedimentary-diagenetic pyrites exhibit high Ni concentrations and low Co/Ni ratios of <1, whereas Co/Ni ratios between 1 and 10 are characteristic of magmatic-hydrothermal pyrite (Bajwah et al., 1987; Reich et al., 2016). The low and restricted range of Co/Ni ratios from Py0 between 0.03 and 1.4 (Fig. 9c), as well as high Ni and Co concentrations, can be interpreted as reflecting a sedimentary-diagenetic origin, which is in agreement with the occurrence of Py0 as disseminated grains in the Ordovician-Silurian Naij Tal Group. Further evidence for a sedimentary-diagenetic origin of Py0 comes from the negative values of $\delta^{34}S$ (−11.6‰ to −4.0‰; Fig. 7). The high concentrations of Co and Ni in Py0 are likely related to high Co and Ni contents in the primary sedimentary environment, reflecting the concentration of these metals by biological processes during sedimentation and diagenesis of organic-rich sediments in an euxinic environment (Coveney, 2000; Alegro and Maynard, 2004; Large et al., 2009), coupled with direct substitution of these metals for $Fe^{2+}$ in the pyrite lattice.

The Py1a sub-type also contains considerable Co and Ni contents, in some cases even higher than Py0 in a single grain (Fig. 10). These high contents of Co and Ni likely resulted from remobilization-redistribution of Co and Ni from earlier Py0. For example, where Py1a was formed by replacement of Py0 via a dissolution-reprecipitation reaction, forming overgrowths on Py0 with irregular contacts (Fig. 10), this Py1a variably inherited the high Co and Ni concentrations from the earlier formed, sedimentary-diagenetic Py0. In contrast, the Py1b sub-type shows relatively low Co and Ni characteristic of hydrothermal pyrite. Hence, the wide range of Co/Ni ratios (0.2–13.8) of Py1 suggests a magmatic-hydrothermal origin but influenced by sedimentary-diagenetic Py0. One exceptional datum with anomalously high Co/Ni ratio (444.2), low Ni and high Co concentrations from Py1 is probably due to micro-inclusions.

Hydrothermal Py2 grains from quartz-pyrite veins exhibit extremely low Co and Ni concentrations and low Co/Ni ratios (0.1–3.0). The dominant range of Co/Ni ratios from Py3 (mostly 0.5–8.5) is consistent

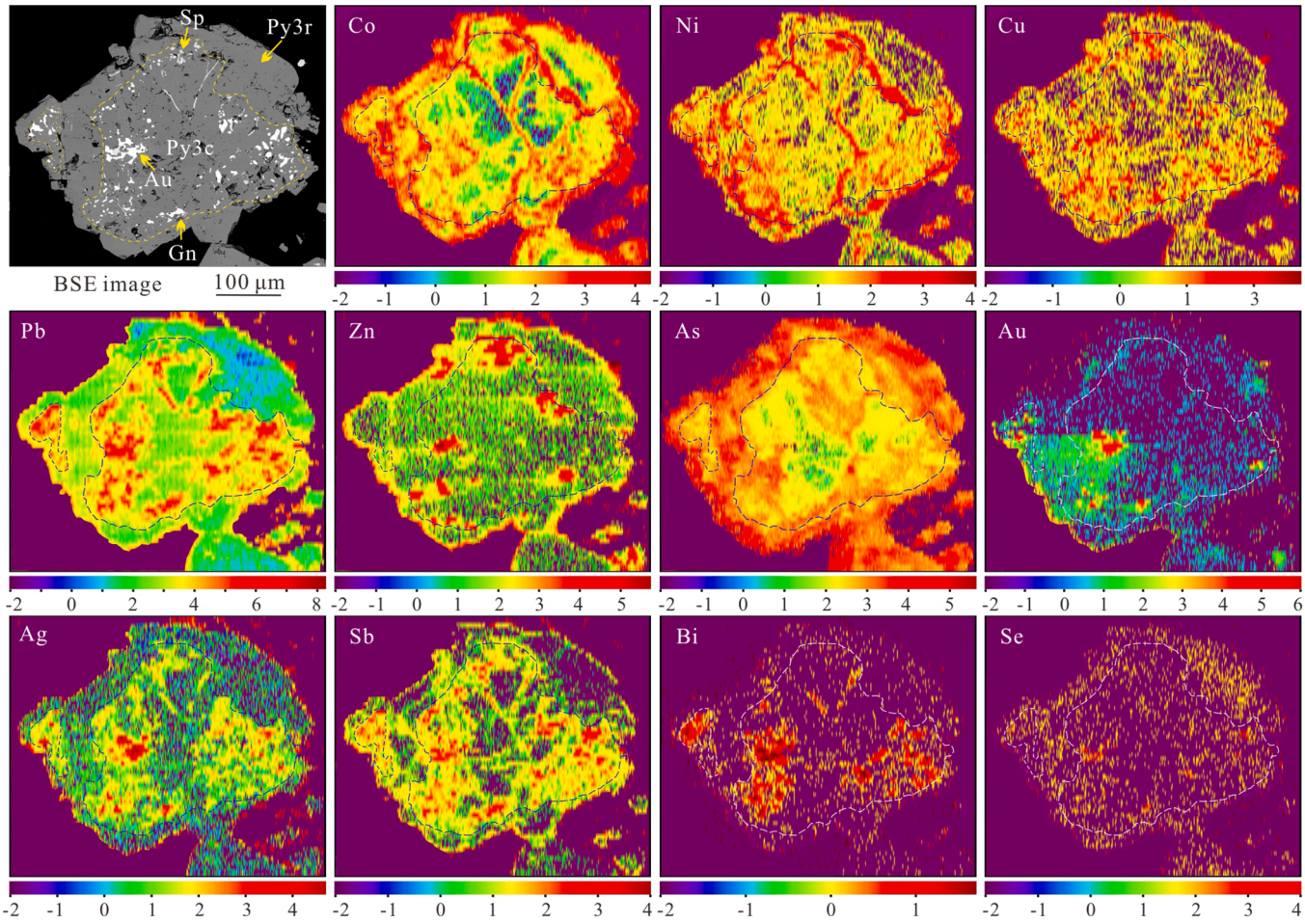


**Fig. 11.** LA-ICPMS trace elemental maps, and a BSE image, of Py3 with an inclusion-rich core (Py3c) and an inclusion-free rim (Py3r). Concentration scales are in ppm (logarithmic $10^n$, where n is given on scale).

with a magmatic-hydrothermal origin (Fig. 9c). The contents of Co and Ni decrease from Py1a through Py1b to Py2, suggesting a trend of hydrothermal fluid evolution; however, these latter metals then increase thereafter through Py3c to Py3r, suggesting a new pulse of ore-forming fluids.

Arsenic is broadly the most abundant trace element in the three generations of hydrothermal pyrite (Py1 to Py3) at Guoluolongwa (Fig. 8), and is generally higher in all three of the latter hydrothermal generations than in the sedimentary-diagenetic Py0. Arsenic ($As^{1-}$) is able to substitute nonstoichiometrically for S2- 2 in the tetrahedral site of pyrite, leading to distortion of the pyrite structure (Simon et al., b, 1999a; Abraitis et al., 2004; Reich et al., 2005, 2013). Structural distortion may allow the incorporation of other trace elements, such as $Au^+$, into the pyrite structure, resulting in a positive correlation between As and other trace elements. The substitution of As for S – as well as the entry of Au – in the pyrite structure is supported by LA-ICPMS data and mapping, which show a negative correlation between As and S and a broadly positive correlation between As and Au, especially for Py1 and Py3r (Fig. 9a, c, 10, and 11). The positive correlation between As and Au indicates that invisible gold occurs as a substituent ($Au^+$) in the pyrite structure, and not as discrete or clustered nanoparticles in Py1 and Py3r (Figs. 10 and 11; Li et al., 2018). The sedimentary-diagenetic Py0, in contrast, has a more restricted range on the As-Au plot due to low concentrations of both elements, compared to the hydrothermal Py1 to Py3.

Other trace metals, including Cu, Pb, Zn, Au, and Ag, also display fundamental differences between Py0, Py1a, Py1b, Py2, Py3c, and Py3r. These metals are depleted in the sedimentary-diagenetic Py0 grains, and even lower (except Au) in hydrothermal Py1a in a single grain (Figs. 8 and 10). In contrast, hydrothermal Py1b, Py2, and Py3r are Cu-Pb-Zn-Au-Ag-rich. Although the concentrations of Cu, Pb, Zn, Au, and Ag in Py3c are low (Fig. 8), abundant inclusions of chalcopyrite, galena, sphalerite, and gold in Py3c indicate the fertility of ore-forming fluids (Fig. 11). The changes in trace metal compositions of the hydrothermal Py1, Py2, and Py3, compared to the sedimentary-diagenetic Py0, is a reflection of the metal solubility and endowment of the ore-forming fluids, and may also be attributed to the ability of the trace elements to substitute for $Fe^{2+}$ and S2- 2 in the pyrite structure at elevated temperatures. In addition, extreme variations of some trace elements such as Cu, Pb, and Zn are present in specific analyses (Supplementary Table 1), and we attribute these exceptionally high values to micro-scale mineral inclusions in pyrite, including chalcopyrite, galena, sphalerite, and gold. Although Ag, Bi, Sb, and Au exhibit only weak to absent correlations (Fig. 9e and f), these elements display systematic variations in the trace elemental maps of Py3c corresponding to the mineral inclusions (Fig. 11). In Py3r, Se shows a positive correlation with As and Au, suggesting that Se may play a role analogous to that of As in substituting and enhancing Au solubility in pyrite (Fig. 11).

### 6.2. *Pyrite paragenesis and ore-forming fluid evolution*

Morphological characteristics, overgrowth relationships, mineral paragenesis, and chemical compositions define a clear paragenetic succession for distinct generations of pyrite at Guoluolongwa, as well as their relationships to quartz veins. This includes pre-ore Py0 in the host phyllite from the Ordovician-Silurian Naij Tal Group; Py1 (Py1a and

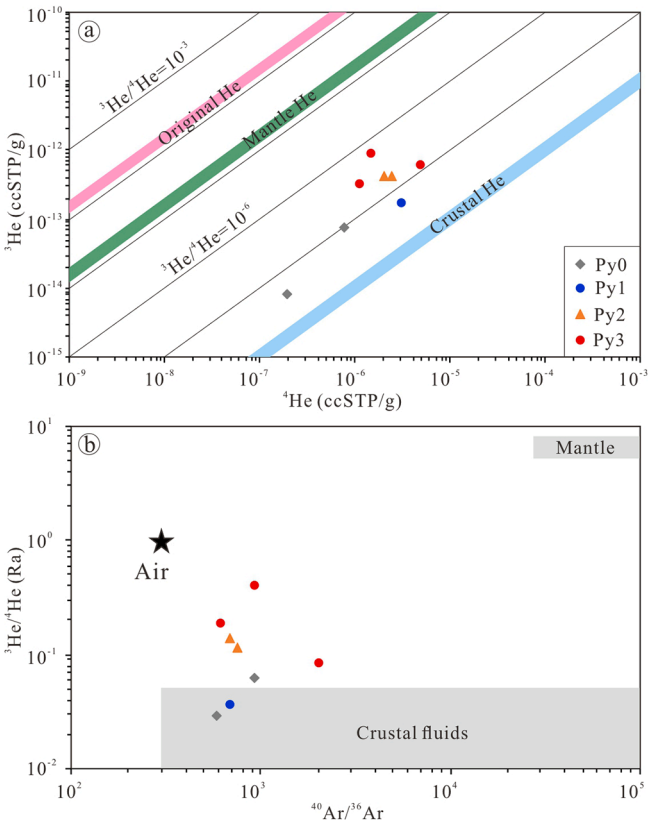


**Fig. 12.** Plots of (**a**) $^3$He versus $^4$He, and (**b**) $^3$He/$^4$He versus $^{40}$Ar/$^{36}$Ar of fluid inclusions in pyrite from the Guoluolongwa gold deposit.

Py1b) in the low-grade pyrite-quartz veins; Py2 in the high-grade quartz-pyrite veins; and Py3 (Py3c and Py3r) in the later high-grade calcite-quartz-sulfide veins that cut the low-grade pyrite-quartz ores.

The textural and chemical differences for the four generations of pyrite indicate different geochemical environment (sedimentary-diagenetic and hydrothermal) and changes in the compositions of hydrothermal fluids, probably involving multiple events (Fig. 13). The sedimentary-diagenetic Py0 grains with silicate-carbonate inclusions, mostly disseminated in the host phyllite, rich in Co and Ni but poor in other metals, pre-date the hydrothermal ore-forming stages. Their chemical compositions and sulfur isotopes reflect sedimentary or diagenetic sulfide formation. Such sedimentary-diagenetic pyrite with highly negative $\delta^{34}$S values has been widely recognized in Paleozoic sedimentary rocks in the Central Orogenic Belt of China (Chang and Chu, 2011; Chen et al., 2015). The formation of Py0 grains, as well as negative $\delta^{34}$S values (−11.6‰ to −4.0‰), can be due to one of or combined mechanisms of (1) microbial sulfate reduction (MSR) in anoxic marine sediments (Fallick et al., 2001), (2) thermochemical sulfate reduction (TSR) at high temperatures during burial diagenesis (Painter et al., 1999), and/or (3) sulfur disproportionation (Fry et al., 1988). The produced hydrogen sulfide reacts with Fe to precipitate pyrite by a series of iron sulfide precursor phases (Raiswell and Berner, 1985).

The occurrence of Py0 veinlets along deformation cleavage of the host rocks (Fig. 3e), and the breakdown texture of primary euhedral Py0 grains in the veinlets (Fig. 6b and e) suggest that Py0 grains were clustered together, forming veinlets, during shear deformation. After Py0 veinlet formation, the stage I ore-forming fluid was introduced, precipitating abundant milky quartz, accompanied by lesser Py1 grains. The host rocks containing Py0 were crosscut and laminated by the quartz veins (Fig. 3f and g), showing evidence of simultaneous shear deformation. As a result, a majority of Py0 veinlets that are proximal to the quartz veins or in the laminations were overprinted by the stage I hydrothermal event, forming overgrowths (Py1a) on Py0. In the overprinting veinlets, Py0 cores usually display irregular shapes and embayments and sharp boundaries with Py1a rims (Fig. 6g, h, and 10), suggesting replacement of Py0 by Py1a via partial dissolution-reprecipitation in the ore-forming fluids. During breakdown and dissolution processes, trace elements (especially Co and Ni, possibly As and minor Au) were released from early pyrite sedimentary-diagenetic Py0 grains, contributing to relatively high concentrations of Co, Ni, and As in Py1a (Fig. 10). The sulfur isotopes of Py1a ($\delta^{34}$S = +1.6‰ to +4.5‰) were also influenced by Py0, resulting in a lower range compared to

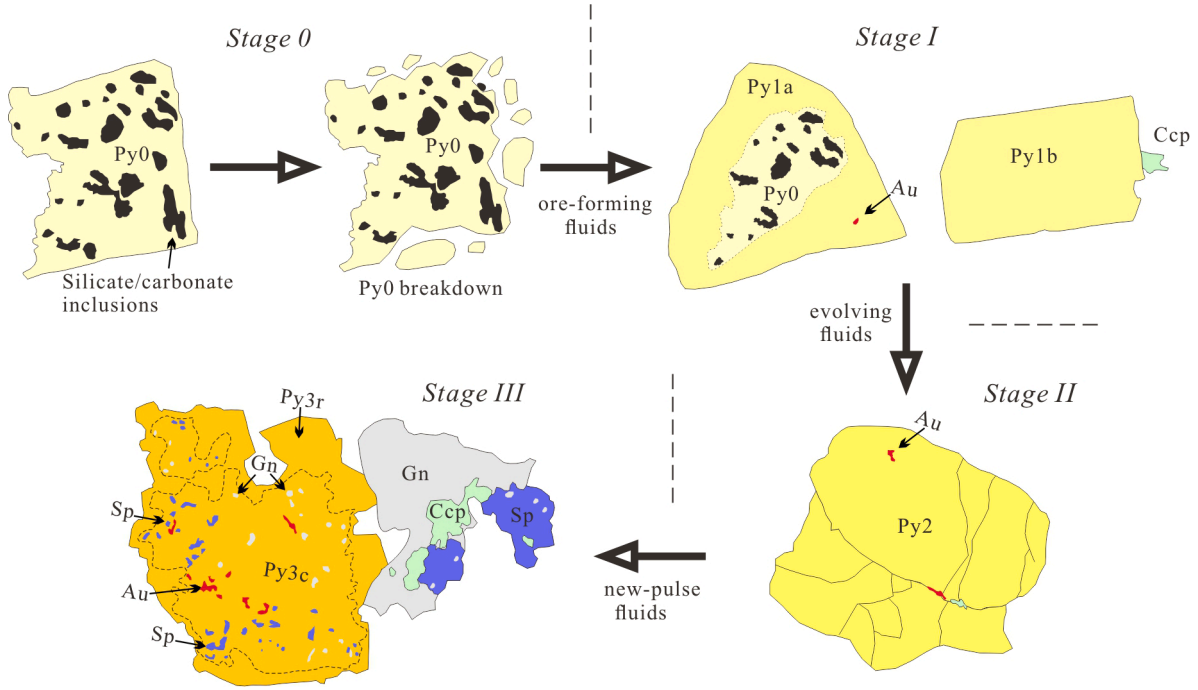


**Fig. 13.** Schematic diagram showing the sequence of formation of the four types of pyrite. *Py* pyrite, *Ccp* chalcopyrite, *Sp* sphalerite, *Gn* galena, *Au* gold.

Py1b ($\delta^{34}S$ = +3.5‰ to +5.6‰; Fig. 7).

The chemical characteristics of primary ore-forming fluids during stage I were represented by the chemistry of Py1b grains, which were sparsely disseminated in quartz veins or occurred as irregular laminae devoid of Py0 influence. According to the trace element contents and sulfur isotopes of Py1b, the initial ore-forming fluid contained relatively low concentrations of Co and Ni, moderate Cu, Pb, Zn, Sb, and Bi, but notably high concentrations of As, Au, and Ag, and relatively high $\delta^{34}S$ values. The homogeneous BSE images indicate that Py1 grains precipitated in a stable environment during stage I (Fig. 6f and h). Minor native gold grains deposited in quartz veins or as inclusions in Py1 (Fig. 5a and b), probably as a result of decompression/cooling-induced saturation under relatively steady conditions during the early ore-forming stage.

Early-stage Py1 shows significant textural and compositional contrasts compared to the subsequent stage (stage II) Py2. Compared to Py1, the subsequent Py2 grains have elevated Cu, Pb, Zn, Ag, and Bi contents, slightly lower Au and As contents, and lower $\delta^{34}S$ values (+1.5‰ to +3.2‰). The Py2 also shows irregular compositional zoning in BSE images (Fig. 6j). These chemical variations can be attributed to phase separation triggered by pressure fluctuation of the ore-forming fluid. Previous studies have proposed that most metals and metalloids (Cu, Pb, Zn, As, Au, and Ag) largely favor partitioning into the liquid over the coexisting vapor phase during vapor–liquid separation (Kouzmanov and Pokrovski, 2012; Román et al., 2019). Fluid phase separation at stage II has been supported by fluid inclusions studies from Chen (2018). Hence, liquid–vapor phase separation would increase the concentrations of dissolved metals in the liquid phase and trigger pyrite deposition, forming abundant metal-rich Py2. During phase separation, reduced gases, such as $H_2$, $CH_4$, and $H_2S$, preferentially partition into the vapor phase, causing an increase of $S^{6+}/S^{2-}$, thus relative oxidation, in residual fluids (Drummond and Ohmoto, 1985). In this case, the resultant pyrite would have lower $\delta^{34}S$ values (Mckibben and Eldridge, 1990; Hodkiewicz et al., 2009; Peterson and Mavrogenes, 2014), consistent with the lower $\delta^{34}S$ of Py2 than Py1. In addition, pressure fluctuation would also promote turbulent flow, which is in agreement with the complex compositional zones on BSE images of Py2. Desulfidation of the ore-forming fluid due to degassing of $H_2S$ and abundant precipitation of Py2 destabilized Au bisulfide complexes but had limited influence on chloride complexes of Cu, Pb, Zn, and Ag (Reed and Palandri, 2006), triggering abundant native Au deposition into fractures and as inclusions in Py2 (Fig. 5c).

The mineral association at stage III contrasts markedly to the prior two stages, most likely implying a new pulse of hydrothermal fluid of different composition (Fig. 13). Chen et al. (2020a) conducted Re-Os dating on pyrite from a quartz-pyrite vein (Py2, stage II) and a polymetallic quartz-sulfide vein (Py3, stage III) in the Guoluolongwa gold deposit, yielding ages of 374 ± 15 Ma and 354 ± 7 Ma, respectively, which were interpreted to record two gold-mineralizing events. Therefore, the chemistry of Py3 (Fig. 8), as well as the coexisting gold, chalcopyrite, sphalerite, and galena, represents a new pulse of Cu-Pb-Zn-As-Au-Ag-rich ore-forming fluid. In addition, the extremely low Bi concentrations in Py3 (Figs. 8 and 9f), which are clearly distinct from the other pyrite types, support that the ore-forming fluid was barren of Bi during stage III. The Py3 grains are characterized by anhedral inclusion-rich cores (Py3c) and clean cubic-pyritohedral rims (Py3r), in which chalcopyrite, galena, sphalerite, and gold occur as inclusions (Fig. 6l and 11). This textural feature is similar to that described by Román et al. (2019), who interpreted the inclusion-rich zones with irregular edges to be a result of abrupt destabilization of metal complexes and rapid precipitation during vigorous boiling (phase separation), whereas the euhedral and pristine rims forming under slower crystallization kinetics and steadier physico-chemical conditions. A similar interpretation may be responsible for the core-rim texture of Py3 from the Guoluolongwa gold deposit. Since stage III ore-forming fluid is expected to be Cu-Pb-Zn-As-Au-Ag-rich, supersaturation conditions may dominate during crystallization of Py3. Vigorous phase separation would effectively destabilize Au-HS and (Cu-Pb-Zn-Ag)-Cl complexes at the same time, contributing to abundant inclusions of native gold, chalcopyrite, galena, and sphalerite in Py3c (Peterson and Mavrogenes, 2014). Rapid co-precipitation of these mineral inclusions is potentially supported by the intimate intergrowth with smooth boundaries (Fig. 5d and e). The subsequent gentle cooling or decompression would drive further dissociation of Au-HS and metal-Cl complexes, precipitating Py3r coexisting with chalcopyrite, sphalerite, and galena (Fig. 3l). Due to the saturation and precipitation of Cu, Pb, and Zn as discrete phases at later stage, the incorporation of these metals, and associated Ag, Sb, and Bi, into Py3r structure was low (Fig. 11). In contrast, the positive correlation and relatively high contents of Co, Ni, As, and Se in Py3r were attributed to the enrichment but undersaturation of these elements in fluids and their strong ability to substitute for $Fe^{2+}$ and S2- 2 in the pyrite structure (Fig. 11; Abraitis et al., 2004; del Real et al., 2020). The coupled behavior of elements promoted more Au incorporation with As into Py3r structure (Fig. 11). This inferred mechanism is compatible with the sulfur isotopes of Py3. The inclusion-rich Py3c cores formed during vigorous phase separation and have relatively low $\delta^{34}S$ values of +0.5‰ to +3.0‰ (e.g., Mckibben and Eldridge, 1990; Hodkiewicz et al., 2009), whereas the clean Py3r rims precipitated under steadier conditions and display slightly higher $\delta^{34}S$ values of +1.9‰ to +3.6‰ (Fig. 7; Supplementary Table 1).

### 6.3. Constraints on the source of sulfur

The isotopic ratios of sulfur ($\delta^{34}S$) in sulfide minerals provide clues to interpret the sulfur source (Seal, 2006; Peterson and Mavrogenes, 2014; Chen et al., 2015). The disseminated Py0 in the host Naij Tal Group displays negative $\delta^{34}S$ values (−11.6‰ to −4.0‰) consistent with a sedimentary-diagenetic origin. The large difference in the sulfur isotopic compositions between Py0 and the subsequent hydrothermal generations of Py1 to Py3 (+0.5‰ to +5.6‰; Fig. 7) from the Guoluolongwa gold deposit indicates that sulfur in the ore-forming fluids was unlikely completely derived from the host rocks during regional metamorphism. A contribution of Py0 dissolution was noted and discussed above, but was highly localized and had limited effect on the sulfur isotopic composition of the bulk of the ore-forming fluids. Compared to the previously reported $\delta^{34}S$ results of bulk pyrite separates (−6.0‰ to +5.2‰; Chen, 2018), *in-situ* analyses in this study constrained the $\delta^{34}S$ of hydrothermal Py1 to Py3 to a narrower range (+0.5‰ to +5.6‰). These positive $\delta^{34}S$ values are consistent with a magmatic source of sulfur (0 ± 5‰; Ohmoto and Rye, 1979; Seal, 2006). Specifically, the $\delta^{34}S$ values of Py1 (+1.6‰ to + 5.6‰) are compatible with those of intermediate to felsic igneous rocks (andesite and granitoids), which have average $\delta^{34}S$ values of 2.6 ± 2.3‰ and 1.0 ± 6.1‰, respectively (Luhr and Logan, 2002; Seal, 2006). Although the $\delta^{34}S$ values of Py2 (+1.5‰ to +3.2‰) and Py3 (+0.5‰ to +3.6‰) are within the range of magmatic rocks, they show slightly lower and more restricted values than Py1, which we attribute to sulfur isotopic fractionation between liquid and vapor during fluid phase separation.

### 6.4. Origin of ore-forming fluids

Helium and Ar isotopic compositions can also be used to determine sources of the mineralizing fluids trapped in the pyrite, after excluding the role of noble gas loss/diffusion, air contamination and *in-situ* noble gas production (Burnard et al., 1999; Tan et al., 2018). Previous work has showed that the effect of noble-gas diffusive loss on the He-Ar isotopic ratio is almost negligible (Burnard et al., 1999; Tan et al., 2018). The calculated $^3He/^{36}Ar$ ($0.06 \times 10^{-4}$–$6.2 \times 10^{-4}$) are much higher than atmosphere or air-saturated water ($5 \times 10^{-8}$), implying that He in the fluids is predominantly non-atmospheric in origin. The in situ noble gas production by radioactive decay of U-Th and K in fluid inclusions can be effectively avoided by multi-step crushing extractions (He et al., 2011).

The $^3He/^4He$ ratios of Py0 (0.03–0.06 Ra) are typical of radiogenic

He in continental crust (0.01–0.05 Ra; Burnard et al., 1999 and references therein), whereas that of Py1-Py3 (0.04–0.4 Ra) are higher than continental crust but notably lower than mantle (6–9 Ra; Burnard et al., 1999 and references therein). On $^{3}He$ versus $^{4}He$ plot (Fig. 12a), samples of Py1-Py3 lie between the crustal and mantle lines and close to the crustal line, indicating mixed sources between the two reservoirs. According to the crust-mantle binary mixing model [$He_{mantle}$ (%) = ($R_S$–$R_C$) / ($R_M$–$R_C$) × 100, in which $R_M$ (=7.5), $R_C$ (=0.03), and $R_S$ (0.04–0.4) represent $^{3}He/^{4}He$ ratios of mantle, crust, and sample, respectively], the proportion of mantle-derived He from the current study is estimated to be lower than 5%.

On the plot of $^{3}He/^{4}He$ versus $^{40}Ar/^{36}Ar$ (Fig. 12b), samples of Py1-Py3 plotted between the air-saturated water and crustal end-members, but far away from the region of mantle fluid. The $^{40}Ar/^{36}Ar$ ratios of Py1-Py3 (623–2081) are in the range of crustal $^{40}Ar/^{36}Ar$ (299–100,000; Kendrick and Burnard, 2013), but higher than the air ratio (295.5; Burnard et al., 1999) and much lower than that of mantle-derived fluids (mostly 30,000–40,000; Kendrick and Burnard, 2013), showing a crustal affinity. In addition, most of the $^{40}Ar^{*}/^{4}He$ ratios are concentrated at 0.2–0.3 which are in coincidence with the average crust (0.2; Torgersen et al., 1989), indicating a crustal source. Two data of Py3 with slightly high $^{40}Ar^{*}/^{4}He$ values of 0.7 and 1.4 are correlated with high radiogenic $^{40}Ar$ (Table 1), which might be attributed to the introduction of more crustal radiogenic $^{40}Ar$ via fluid/wall-rock interaction. Another alternative explanation for the high $^{40}Ar^{*}/^{4}He$ values of Py3 is He/Ar fractionation during boiling. Since Ar is more soluble in aqueous fluids than He, Ar/He of the remaining liquid is likely to increase during boiling (Burnard et al., 1999 and references therein), consistent with the vigorous phase separation illustrated by Py3 texture and chemistry. The $^{40}Ar^{*}/^{4}He$ ratios of Py1-Py3 are much higher than that of air-saturated water (0.01; Burnard et al., 1999), implying negligible contribution of atmospheric compositions.

Analyses of noble gases from the Guoluolongwa gold deposit demonstrate that the ore-forming fluids were mainly derived from a crustal source with minor contributions of mantle components. As outlined in the previous section, the S isotopic composition of the hydrothermal pyrite generations Py1 through Py3 suggests a magmatic sulfur source. Combined, these two lines of evidence suggest that the ore-forming fluids were exsolved from crustal-derived felsic magmas, permissibly with a lesser contribution from mantle-derived mafic magma. During migration through the crust, the ore-forming fluids likely interacted with wall-rock, extracting He and Ar and acquiring a more radiogenic He and Ar isotopic signature. A magmatic-hydrothermal fluid source is further supported by previous H-O isotopic data that suggested a magmatic origin for the ore-forming fluids (Xiao et al., 2014). The broadly low contents of Co and Ni in the hydrothermal pyrite (Py1-Py3) from the Guoluolongwa gold deposit are generally interpreted as an indicator of felsic magmatic-hydrothermal affinity (Bajwah et al., 1987; Large et al., 2009; Reich et al., 2016). This interpretation is also in agreement with the extensive distribution of Paleozoic dioritic and granitic intrusions (466–390 Ma; Dong et al., 2018; slightly earlier than the pyrite Re-Os age at 374–354 Ma by Chen et al., 2020a), and Triassic granitoids with mafic magmatic enclaves, which were generated via partial melting of crust with inherited mantle isotopic signatures (257–200 Ma; Shao et al., 2017; Dong et al., 2018; Zhao et al., 2020; contemporaneous with the sericite / muscovite Ar-Ar age at ca. 203 Ma for the Guoluolongwa gold deposit by Xiao et al., 2014), in the eastern Central East Kunlun Belt. However, due to the uncertainty of metallogenic age (Paleozoic or Triassic) for the Guoluolongwa gold deposit, we cannot pinpoint the causative magmas at present. Furthermore, multiple ore-forming stages revealed in this study, as well as an age gap of ca. 20 Ma constrained by Re-Os geochronology of Py2 and Py3 (Chen et al., 2020a), potentially imply multiple mineralizing events which may be related to multiple episodes of magmatism in the Gouli goldfield.

## 7. Conclusions

The Guoluolongwa gold deposit contains four generations of pyrite, including an early sedimentary-diagenetic variety Py0 and three later hydrothermal generations Py1 to Py3. The Py0 showed clearly distinct trace elements and sulfur isotopes compared to the subsequent hydrothermal pyrite. Early Py0 is partly replaced by Py1a and conferred Co, Ni, and As, as well as sulfur isotopes to this first hydrothermal pyrite. Next, Py1b was deposited in pyrite-quartz veins during stage I, representing initial fluid composition with low concentrations of Co and Ni, moderate Cu, Pb, Zn, Sb, and Bi, but high As, Au, and Ag. Following fluid phase separation, likely driven by pressure fluctuations, the concentrations of trace metals in the ore-forming fluid phase increased, but the sulfur isotopic values ($\delta^{34}S$) decreased, precipitating abundant Py2 and further triggering native Au deposition due to desulfidation during stage II. During stage III, Py3 was deposited in polymetallic sulfides-calcite-quartz veins. We infer that Py3 represents a new pulse of Cu-Pb-Zn-As-Au-Ag-rich and Bi-poor ore-forming fluid. The inclusion-rich Py3c cores likely formed as a result of abrupt destabilization of metal complexes and rapid precipitation, which was thus accompanied by abundant chalcopyrite, galena, sphalerite, and native gold during vigorous phase separation. In contrast, the euhedral Py3r rims formed under steadier physico-chemical conditions with slower crystallization kinetics. Sulfur isotopes and He-Ar isotopic analyses of pyrite are consistent with a model in which multiple pulse of ore-forming fluids in the Guoluolongwa gold deposit were predominantly exsolved from crustal-derived felsic magmas with lesser input of mantle-derived components, in accord with widespread granitoid magmatism in the eastern Central East Kunlun Belt.

## Declaration of Competing Interest

The authors declare that they have no known competing financial interests or personal relationships that could have appeared to influence the work reported in this paper.

## Acknowledgments

We thank Weiqiang Sun from the Qinghai Shanjin Mining Co., Ltd., for help during our field work; and Zhihui Dai, Zheng Liu and Fei Su for their technical support in running the LA-ICPMS, LA-MC-ICPMS and He-Ar isotopic analyses. We thank two anonymous reviewers for their insightful comments and detailed reviews, which improved the quality of this manuscript. We acknowledge Associate Editor Prof. Santosh for his very helpful suggestions and efficient handling. This work was funded by the Second Tibetan Plateau Scientific Expedition and Research Program (STEP) (No. 2019QZKK0801), National Natural Science Foundation of China (No. 42002078), and China Postdoctoral Science Foundation (No. 2019M660788).

## References

Abraitis, P.K., Pattrick, R.A.D., Vaughan, D.J., 2004. Variations in the compositional, textural and electrical properties of natural pyrite: A review. Int. J. Miner. Process. 74 (1-4), 41–59.

Bajwah, Z.U., Seccombe, P.K., Offler, R., 1987. Trace element distribution Co: Ni ratios and genesis of the Big Cadia iron-copper deposit, New South Wales, Australia. Miner. Deposita 22, 292–300.

Barker, S.L.L., Hickey, K.A., Cline, J.S., Dipple, G.M., Kilburn, M.R., Vaughan, J.R., Longo, A.A., 2009. Uncloaking invisible gold: use of nano-SIMS to evaluate gold, trace elements, and sulfur isotopes in pyrite from Carlin-type gold deposits. Econ. Geol. 104 (7), 897–904.

Bian, Q.-T., Li, D.-H., Pospelov, I., Yin, L.-M., Li, H.-S., Zhao, D.-S., Chang, C.-F., Luo, X.-Q., Gao, S.-L., Astrakhantsev, O., Chamov, N., 2004. Age, geochemistry and tectonic setting of Buqingshan ophiolites, North Qinghai-Tibet Plateau, China. J. Asian Earth Sci. 23 (4), 577–596.

Bralia, A., Sabatini, G., Troja, F., 1979. A revaluation of the Co/Ni ratio in pyrite as geochemical tool in ore genesis problems. Miner. Deposita 14, 353–374.

Burnard, P.G., Hu, R.Z., Turner, G., Bi, X.W., 1999. Mantle, crustal and atmospheric noble gases in Ailaoshan gold deposit, Yunnan province, China. Geochim. Cosmochim. Acta 63, 1595–1604.
Campbell, F.A., Ethier, V.G., 1984. Nickel and colbalt in pyrrhotite and pyrite from the Faro and Sullivan ore bodies. The Canadian Mineralogist 22, 503–506.
Chang, H., Chu, X., 2011. Pyrite framboids and palaeo-ocean redox condition reconstruction. Advances in Earth Science 26, 475–481 (in Chinese with English abs.).
Chen, J., Wei, J., Fu, L., Li, H., Zhou, H., Zhao, X.u., Zhan, X., Tan, J., 2017. Multiple sources of the Early Mesozoic Gouli batholith, Eastern Kunlun Orogenic Belt, northern Tibetan Plateau: Linking continental crustal growth with oceanic subduction. Lithos 292-293, 161–178.
Chen, J., 2018. Paleozoic-Mesozoic tectono-magmatic evolution and gold mineralization in Gouli Area, east end of East Kunlun Orogen: Ph.D. thesis. China University of Geosciences, Wuhan (in Chinese with English abs.).
Chen, J., Fu, L., Selby, D., Wei, J., Zhao, X.u., Zhou, H., 2020a. Multiple episodes of gold mineralization in the East Kunlun Orogen, western Central Orogenic Belt, China: Constraints from Re-Os sulfide geochronology. Ore Geol. Rev. 123, 103587. https://doi.org/10.1016/j.oregeorev.2020.103587.
Chen, J., Fu, L., Wei, J., Selby, D., Zhang, D., Zhou, H., Zhao, X.u., Liu, Y., 2020b. Proto-Tethys magmatic evolution along northern Gondwana: Insights from Late Silurian-Middle Devonian A-type magmatism, East Kunlun Orogen, Northern Tibetan Plateau. China. Lithos 356-357, 105304. https://doi.org/10.1016/j.lithos.2019.105304.
Chen, L., Sun, Y., Pei, X., Gao, M., Feng, T., Zhang, Z., Chen, W., 2001. Northernmost Paleo-Tethyan oceanic basin in Tibet: geochronological evidence from 40Ar/39Ar age dating of Dur'ngoi ophiolite. Chin. Sci. Bull. 46 (14), 1203–1205.
Chen, L., Li, X.-H., Li, J.-W., Hofstra, A.H., Liu, Y.u., Koenig, A.E., 2015. Extreme variation of sulfur isotopic compositions in pyrite from the Qiuling sediment-hosted gold deposit, West Qinling orogen, central China: an in situ SIMS study with implications for the source of sulfur. Miner. Deposita 50 (6), 643–656.
Chen, N.S., Sun, M., Wang, Q.Y., Zhao, G.C., Chen, Q., Shu, G.M., 2007. EMP chemical ages of monazites from Central Zone of the eastern Kunlun Orogen: records of multi-tectonometamorphic events. Chinese Science Bulletin 52, 2252–2263.
Chen, Y.X., Pei, X.Z., Li, R.B., Li, Z.C., Pei, L., Chen, G.C., Liu, C.J., Li, X.B., Yang, J., 2013. Zircon U-Pb age, geochemical and tectonic significance of metavolcanic rocks from Naij Tal Group, east section of east Kunlun. Earth Sci. Front. 20, 240–254 (in Chinese with English abs.).
Coveney, R.M., 2000. Metalifferous shales and the role of organic matter, with examples from China, Poland, and the United States: A review. Econ. Geol. 95, 251–280.
Danyushevsky, L., Robinson, P., Gilbert, S., Norman, M., Large, R., McGoldrick, P., Shelley, M., 2011. Routnie quantitative multi-element analysis of sulphide minerals by laser ablation ICP-MS: Standard development and consideration of matrix effects. Geochem.-Explor. Environ. Anal. 11, 51–60.
Davis, B.K., Hippertt, J.F.M., 1998. Relationships between gold concentration and structure in quartz veins from the Hodgkinson Province, northeastern Australia. Miner. Deposita 33 (4), 391–405.
Deditius, A.P., Reich, M., Kesler, S.E., Utsunomiya, S., Chryssoulis, S.L., Walshe, J., Ewing, R.C., 2014. The coupled geochemistry of Au and As in pyrite from hydrothermal ore deposits. Geochim. Cosmochim. Acta 140, 644–670.
del Real, I., Thompson, J.F.H., Simon, A.C., Reich, M., 2020. Geochemical and Isotopic Signature of Pyrite as a Proxy for Fluid Source and Evolution in the Candelaria-Punta del Cobre Iron Oxide Copper-Gold District, Chile. Econ. Geol. 115, 1493–1517.
Ding, Q.F., Jin, S.K., Wang, G., Zhang, B.L., 2013. Ore-forming fluid of the Guoluolongwa gold deposit in Dulan county, Qinghai province. J. Jilin Univ. (Earth Sci. Ed.) 43, 415–426 (in Chinese with English abs.).
Dong, Y., He, D., Sun, S., Liu, X., Zhou, X., Zhang, F., Yang, Z., Cheng, B., Zhao, G., Li, J., 2018. Subduction and accretionary tectonics of the East Kunlun orogen, western segment of the Central China Orogenic System. Earth Sci. Rev. 186, 231–261.
Drummond, S.E., Ohmoto, H., 1985. Chemical evolution and mineral deposition in boiling hydrothermal systems. Economic Geology 80, 126–147.
Fallick, A.E., Ashton, J.H., Boyce, A.J., Ellam, R.M., Russell, M.J., 2001. Bacteria were responsible for the magnitude of the world-class hydrothermal base metal sulfide orebody at Navan, Ireland. Econ. Geol. 96, 885–890.
Feng, C.Y., 2002. Multiple orogenic processes and mineralization of orogenic gold deposits in the East Kunlun Orogen, Qinghai Province: Ph.D. thesis. Chinese Academy of Geological Sciences, Beijing 104p (in Chinese with English abs.).
Fry, B., Gest, H., Hayes, J.M., 1988. $^{34}S/^{32}S$ fractionation in sulfur cycles catalyzed by anaerobic bacteria. Appl. Environ. Microbiol. 54, 250–256.
Fu, J., Hu, Z., Zhang, W., Yang, L.u., Liu, Y., Li, M., Zong, K., Gao, S., Hu, S., 2016. In situ, sulfur isotopes ($\delta^{34}S$ and $\delta^{33}S$) analyses in sulfides and elemental sulfur using high sensitivity cones combined with the addition of nitrogen by Laser Ablation MC-ICP-MS. Anal. Chim. Acta 911, 14–26.
Gilbert, S.E., Danyushevsky, L.V., Rodemann, T., Shimizu, N., Gurenko, A., Meffre, S., Thomas, H., Large, R.R., Death, D., 2014. Optimisation of laser parameters for the analysis of sulphur isotopes in sulphide minerals by laser ablation ICP-MS. J. Anal. At. Spectrom. 29 (6), 1042–1051.
Goldfarb, R.J., Groves, D.I., Gardoll, S., 2001. Orogenic gold and geologic time: a global synthesis. Ore Geol. Rev. 18 (1-2), 1–75.
Goldfarb, R.J., Groves, D.I., 2015. Orogenic gold: common or evolving fluid and metal sources through time. Lithos 233, 2–26.
Groves, D.I., Goldfarb, R.J., Gebre-Mariam, M., Hagemann, S.G., Robert, F., 1998. Orogenic gold deposits: a proposed classification in the context of their crustal distribution and relationship to other gold deposit types. Ore Geol. Rev. 13 (1-5), 7–27.
Groves, D.I., Goldfarb, R.J., Santosh, M., 2016. The conjunction of factors that lead to formation of giant gold provinces and deposits in non-arc settings. Geosci. Front. Special Issue 7 (3), 303–314.
Groves, D.I., Santosh, M., 2020. Craton and thick lithosphere margins: The site of giant mineral deposits and mineral provinces. Gondwana Res. https://doi.org/10.1016/j.gr.2020.06.008.
Groves, D.I., Santosh, M., Deng, J., Wang, Q., Yang, L., Zhang, L., 2020. A holistic model for the origin of orogenic gold deposits and its implications for exploration. Miner. Deposita 55 (2), 275–292.
He, H., Zhu, R., Saxton, J., 2011. Noble gas isotopes in corundum and peridotite xenoliths from the eastern North China Craton: implication for comprehensive refertilization of lithospheric mantle. Phys. Earth Planet. Inter. 189 (3-4), 185–191.
Hodkiewicz, P.F., Groves, D.I., Davidson, G.J., Weinberg, R.F., Hagemann, S.G., 2009. Influence of structural setting on sulphur isotopes in Archean orogenic gold deposits, Eastern Goldfields Province, Yilgarn, Western Australia. Miner. Deposita 44 (2), 129–150.
Hu, Z., Zhang, W., Liu, Y., Gao, S., Li, M., Zong, K., Chen, H., Hu, S., 2015. "Wave" signal-smoothing and mercury-removing device for laser ablation quadrupole and multiple collector ICPMS analysis: application to lead isotope analysis. Anal. Chem. 87 (2), 1152–1157.
Huang, H., Niu, Y., Nowell, G., Zhao, Z., Yu, X., Zhu, D.-C., Mo, X., Ding, S., 2014. Geochemical constraints on the petrogenesis of granitoids in the East Kunlun Orogenic belt, northern Tibetan Plateau: implications for continental crust growth through syn-collisional felsic magmatism. Chem. Geol. 370, 1–18.
Jiang, C.F., Yang, J.S., Feng, B.G., Zhu, Z.Z., Zhao, M., Chai, Y.C., Shi, X.D., Wang, H.D., Hu, J.Q., 1992. Opening-Closing Tectonics of Kunlun Mountains. Geological Publishing House, Beijing 1–224 (in Chinese with English abs.).
Jiang, C.F., Wang, Z.Q., Li, J.Y., 2000. Opening-Closing Tectonics of Central China Orogenic Belt. Geological Publishing House, Beijing 1–107 (in Chinese).
Kendrick, M.A., Burnard, P.G., 2013. Noble gases and halogens in fluid inclusions: a journey through the earth's crust. In: The Noble Gases as Geochemical Tracers, pp: 319–369.
Kouzmanov, K., Pokrovski, G.S., 2012. Hydrothermal controls on metal distribution in porphyry Cu (-Au-Mo) systems. Special Publications of the Society of Economic Geologists 16, 573–618.
Large, R.R., Danyushevsky, L., Hollit, C., Maslennikov, V., Meffre, S., Gilbert, S., Bull, S., Scott, R., Emsbo, P., Thomas, H., Singh, B., Foster, J., 2009. Gold and trace element zonation in pyrite using a laser imaging technique: Implications for the timing of gold in orogenic and Carlin-style sediment-hosted deposits. Econ. Geol. 104 (5), 635–668.
Large, R.R., Bull, S.W., Maslennikov, V.V., 2011. A carbonaceous sedimentary source-rock model for Carlin-type and orogenic gold deposits. Econ. Geol. 106 (3), 331–358.
Li, J., 2017. Metallogenic regularity and metallogenic prognosis of gold deposit in the East Kunlun Orogen, Qinghai Province: Ph.D. thesis. Chang'an University, Xi'an (in Chinese with English abs.).
Li, X.H., Fan, H.R., Yang, K.F., Hollings, P., Liu, X., Hu, F.F., Cai, Y.C., 2018. Pyrite textures and compositions from the Zhuangzi Au deposit, southeastern North China craton: Implication for ore-forming processes. Contrib. Miner. Petrol. 73, 73.
Liu, Y., Hu, Z., Gao, S., Günther, D., Xu, J., Gao, C., Chen, H., 2008. In situ analysis of major and trace elements of anhydrous minerals by LA-ICP-MS without applying an internal standard. Chem. Geol. 257 (1-2), 34–43.
Liu, Z.Q., Pei, X.Z., Li, R.B., Li, Z.C., Chen, Y.X., Gao, J.M., Liu, C.J., Wang, X.L., Wei, F. G., Zhang, G., Yang, Z.Z., 2011. Geological characteristics of the Buqingshan tectonics mélange belt in the southern margin of east Kunlun and its tectonic implications. Geological Bulletin of China 30, 1182–1195 (in Chinese with English abs.).
Luhr, J.F., Logan, M.A.V., 2002. Sulfur isotope systematics of the 1982 El Chichón trachyandesite: an ion microprobe study. Geochim. Cosmochim. Acta 66 (18), 3303–3316.
Matsuda, J., Matsumoto, T., Sumino, H., Nagao, K., Yamamoto, J., Miura, Y., Kaneoka, I., Takahata, N., Sano, Y., 2002. The $^{3}He/^{4}He$ ratio of the new internal He standard of Japan (HESJ). Geochem. J. 36 (2), 191–195.
McKibben, M.A., Eldridge, C.S., 1990. Radical sulfur isotope zonation of pyrite accompanying boiling and epithermal gold deposition; a SHRIMP study of the Valles Caldera, New Mexico. Economic Geology 85, 1917–1925.
Meng, F.C., Cui, M.H., Wu, X.K., Wu, J.F., Wang, J.H., 2013. Magmatic and metamorphic events recorded in granitic gneisses from the Qimantag, East Kunlun Mountains, Northwest China. Acta Petrol. Sin. 29, 2107–2122 (in Chinese with English abs.).
Mo, X.X., Luo, Z.H., Deng, J.F., Yu, X.H., Liu, C.D., Chen, H.W., Yuan, W.M., Liu, Y.H., 2007. Granitoids and crustal growth in the East-Kunlun Orogenic Belt. Geol. J. China Univ. 13, 403–414 (in Chinese with English abs.).
Ohmoto, H., Rye, R.O., 1979. Isotopes of sulfur and carbon. In: Barnes, H.L. (Ed.), Geochemistry of Hydrothermal Ore Deposits. John Wiley and Sons, pp. 509–567.
Painter, M.G.M., Golding, S.D., Hannan, K.W., Neudert, M.K., 1999. Sedimentologic, petrographic, and sulfur isotope constraints on fine-grained pyrite formation at Mount Isa mine and environs, Northwest Queensland, Australia. Economic Geology 94, 883–912.
Patten, C.G.C., Pitcairn, I.K., Molnár, F., Kolb, J., Beaudoin, G., Guilmette, C., Peillod, A., 2020. Gold mobilization during metamorphic devolatilization of Archean and Paleoproterozoic metavolcanic rocks. Geology 48, 1110–1114.
Peterson, E., Mavrogenes, J., 2014. Linking high-grade gold mineralization to earthquake-induced fault-valve processes in the Porgera gold deposit, Papua New Guinea. Geology 42, 383–386.
Phillips, G.N., Powell, R., 2009. Formation of gold deposits–review and evaluation of the continuum model. Earth Sci. Rev. 94 (1-4), 1–21.

Raiswell, R., Berner, R.A., 1985. Pyrite formation in euxinic and semi-euxinic sediments. Am. J. Sci. 285 (8), 710–724.
Reed, M.H., Palandri, J., 2006. Sulfide mineral precipitation from hydrothermal fluids. Rev. Mineral. Geochem. 61, 609–631.
Reich, M., Kesler, S.E., Utsunomiya, S., Palenik, C.S., Chryssoulis, S.L., Ewing, R.C., 2005. Solubility of gold in arsenian pyrite. Geochim. Cosmochim. Acta 69 (11), 2781–2796.
Reich, M., Deditius, A., Chryssoulis, S., Li, J.-W., Ma, C.-Q., Parada, M.A., Barra, F., Mittermayr, F., 2013. Pyrite as a record of hydrothermal fluid evolution in a porphyry copper system: A SIMS/EMPA trace element study. Geochim. Cosmochim. Acta 104, 42–62.
Reich, M., Simon, A.C., Deditius, A., Barra, F., Chryssoulis, S., Lagas, G., Tardani, D., Knipping, J., Bilenker, L., Sánchez-Alfaro, P., Roberts, M.P., Munizaga, R., 2016. Trace element signature of pyrite from the Los Colorados iron oxide-apatite (IOA) deposit, Chile: A missing link between Andean IOA and iron oxide copper-gold systems? Econ. Geol. 111 (3), 743–761.
Ridley, J.R., Diamond, L.W., 2000. Fluid chemistry of orogenic lode gold deposits and implications for genetic models. Rev. Econ. Geol. 13, 141–162.
Román, N., Reich, M., Leisen, M., Morata, D., Barra, F., Deditius, A.P., 2019. Geochemical and micro-textural fingerprints of boiling in pyrite. Geochim. Cosmochim. Acta 246, 60–85.
Seal, R.R., 2006. Sulfur isotope geochemistry of sulfide minerals. Rev. Mineral. Geochem. 61 (1), 633–677.
Shao, F., Niu, Y., Liu, Y.i., Chen, S., Kong, J., Duan, M., 2017. Petrogenesis of Triassic granitoids in the East Kunlun Orogenic Belt, northern Tibetan Plateau and their tectonic implications. Lithos 282-283, 33–44.
Simon, G., Huang, H., Penner-Hahn, J.E., Kesler, S.E., Kao, L.-S., 1999a. Oxidation state of gold and arsenic in gold-bearing arsenian pyrite. Am. Mineral. 84 (7-8), 1071–1079.
Simon, G., Kesler, S.E., Chryssoulis, S., 1999b. Geochemistry and textures of gold-bearing arsenian pyrite, Twin Creeks, Nevada: Implications for deposition of gold in Carlin-type deposits. Economic Geology 94, 405–421.
Tan, J., Wei, J., He, H., Su, F., Li, Y., Fu, L., Zhao, S., Xiao, G., Zhang, F., Xu, J., Liu, Y., Stuart, F.M., Zhu, R., 2018. Noble gases in pyrites from the Guocheng-Liaoshang gold belt in the Jiaodong province: evidence for a mantle source of gold. Chem. Geol. 480, 105–115.
Tanner, D., Henley, R.W., Mavrogenes, J.A., Holden, P., 2016. Sulfur isotope and trace element systematics of zoned pyrite crystals from the El Indio Au–Cu–Ag deposit, Chile. Contrib. Mineral. Petrol. 171, 33.
Tardani, D., Reich, M., Deditius, A.P., Chryssoulis, S., Sánchez-Alfaro, P., Wrage, J., Roberts, M.P., 2017. Copper-arsenic decoupling in an active geothermal system: A link between pyrite and fluid composition. Geochim. Cosmochim. Acta 204, 179–204.
Torgersen, T., Kennedy, B.M., Hiyagon, H., Chiou, K.Y., Reynolds, J.H., Clarke, W.B., 1989. Argon accumulation and the crustal degassing flux of $^{40}$Ar in the Great Artesian Basin, Australia. Earth Planet. Sci. Lett. 92 (1), 43–56.
Tomkins, A.G., 2013. On the source of orogenic gold. Geology 41, 1255–1256.
Wang, G.C., Chen, N.S., Zhu, Y.H., Zhang, K.X., 2003. Late Caledonian ductile thrusting deformation in the Central East Kunlun Belt, Qinghai, China and its significance: evidence from geochronology. Acta Geol. Sin. 77, 311–319.
Weatherley, D.K., Henley, R.W., 2013. Flash vaporization during earthquakes evidenced by gold deposits. Nat. Geosci. 6 (4), 294–298.
Xia, R., Wang, C., Qing, M., Li, W., Carranza, E.J.M., Guo, X., Ge, L., Zeng, G., 2015. Zircon U-Pb dating, geochemistry and Sr-Nd-Pb-Hf-O isotopes for the Nan'getan granodiorites and mafic microgranular enclaves in the East Kunlun Orogen: record of closure of the Paleo-Tethys. Lithos 234-235, 47–60.
Xiao, Y., Feng, C.Y., Li, D.X., Liu, J.N., 2014. Chronology and fluid inclusions of the Guoluolongwa gold deposit in Qinghai province. Acta Geol. Sin. 88, 895–902 (in Chinese with English abs.).
Yang, J.-S., Robinson, P.T., Jiang, C.-F., Xu, Z.-Q., 1996. Ophiolites of the Kunlun Mountains, China and their tectonic implications. Tectonophysics 258 (1-4), 215–231.
Yin, A.n., Harrison, T.M., 2000. Geologic evolution of the Himalayan-Tibetan orogen. Annu. Rev. Earth Planet. Sci. 28 (1), 211–280.
Zhang, D.Q., Dang, X.Y., She, H.Q., Li, D.X., Feng, C.Y., Li, J.W., 2005. Ar-Ar dating of orogenic gold deposits in northern margin of Qaidam and East Kunlun Mountains and its geological significance. Mineral Deposits 24, 87–98 (in Chinese with English abs.).
Zhang, J., Ma, C., Xiong, F., Liu, B., Li, J., Pan, Y., 2014. Early Paleozoic high-Mg diorite-granodiorite in the eastern Kunlun Orogen, western China: response to continental collision and slab break-off. Lithos 210-211, 129–146.
Zhang, J., Ma, C., Li, J., Pan, Y., 2017. A possible genetic relationship between orogenic gold mineralization and post-collisional magmatism in the eastern Kunlun Orogen, western China. Ore Geol. Rev. 81, 342–357.
Zhao, C.S., 2004. Gold, silver metallogeny in Eastern Kunlun Orogenic Belt, Qinghai Province: Ph.D. thesis. Jilin University, Changchun (in Chinese with English abs.).
Zhao, X.u., Fu, L., Wei, J., Bagas, L., Santosh, M., Liu, Y., Zhang, D., Zhou, H., 2019. Late Permian back-arc extension of the eastern Paleo-Tethys Ocean: Evidence from the East Kunlun Orogen, northern Tibetan Plateau. Lithos 340-341, 34–48.
Zhao, X.u., Wei, J., Fu, L., Huizenga, J.M., Santosh, M., Chen, J., Wang, D., Li, A., 2020. Multi-stage crustal melting from Late Permian back-arc extension through Middle Triassic continental collision to Late Triassic post-collisional extension in the East Kunlun Orogen. Lithos 360-361, 105446. https://doi.org/10.1016/j.lithos.2020.105446.
Zou, D.X., Yang, X.B., Lu, W.Q., 2011. Isotope characteristic and ore genesis of Guoluolongwa gold deposit in Qinghai province. Gold Sci. Technol. 19, 26–30 (in Chinese with English abs.).